Detection and Control of Individual Trapped Ions and Neutral Atoms

by

Mark Acton

A dissertation submitted in partial fulfillment
of the requirements for the degree of
Doctor of Philosophy
(Physics)
in The University of Michigan
2008

Doctoral Committee:

Professor Christopher R. Monroe, University of Maryland, Co-Chair
Professor Georg A. Raithel, Co-Chair
Professor Dante E. Amidei
Professor Paul R. Berman
Professor Duncan G. Steel

To Sara and Loie

ACKNOWLEDGEMENTS

Experimental physics research is the ultimate group activity where each person's effort is just part of a larger project. This could not be any more true for the work described here and I would like to try to thank everyone involved in making it possible.

It only makes sense to start by thanking Chris Monroe for serving as my thesis advisor. When I arrived at Michigan in September 2003 he was open to me starting work in the group even as my class commitments kept me busy. He allowed us to be incredibly productive in lab by providing all the financial and logistical support we needed. He also made it incredibly challenging by always pushing us to go farther and faster. Chris did it all as a thesis advisor and this would not have been possible without him.

My thesis committee (Georg Raithel, Dan Amidei, Paul Berman, and Duncan Steel) have been wonderfully supportive and accomodating throughout moves, delays, and scheduling. And while he may not be on my official committee, I would like to thank Jens Zorn for his constant encouragement and support during the inevitable ups and downs of research.

My immediate research group has evolved over the years, but it has always been a source of knowledge and enjoyment. Paul Haljan, Ming-Shien Chang, and Winni Hensinger have served as outstanding mentors and post-docs. Kathy-Anne Brick-

man, Patty Lee, Louis Deslauriers, and Dan Stick have been the best of fellow graduate students. Dave Hucul, Mark Yeo, Andrew Chew, Rudy Kohn, Liz Otto, and Dan Cook brought great energy and initiative as undergraduates. And a big thank you to all those in the group with whom I may not have officially collaborated, but from whom I certainly benefited: David Moehring, Martin Madsen, Steve Olmschenk, Boris Blinov, Peter Maunz, Dzimitry Matsukevich, Jon Sterk, Simcha Korenblit, and Yisa Rumala.

I would like to thank the FOCUS center for fellowship support during my first year as well as conference assistance throughout my graduate school career and the University of Michigan Physics Department for its final term dissertation support. I also thank Deerfield Academy for its financial support and the faculty for their motivation throughout the writing process.

My surrounding family, from my parents and brother to my wonderful in-laws, has provided confidence, praise, and motivation from the beginning. Thank you.

I have saved thanking my wife and daughter until the very end, hoping that I would be less emotional and better able to put into words how much their support has meant during this odyssey. Of course, I now realize that I will never be able to adequately thank them. They provided motivation, encouragement, and relaxation. From late nights to early mornings (and sometimes the spaces in between), Sara was always ready to bend her schedule to keep us from breaking. She defines generosity and I hope that this product is at least partially worthy of her investment.

TABLE OF CONTENTS

LIST OF FIGURES

Figure

LIST OF APPENDICES

Appendix

ABSTRACT

Significant interest and effort have been devoted to using quantum mechanics in order to perform quantum computations or model quantum mechanical systems. Using trapped atomic ions as the building block for a quantum information processor has found notable success, but important questions remain about methods for achieving acceptable error rates in qubit measurement and entanglement production as well as increasing the number of controlled qubits. In this work we present a detailed discussion of qubit measurement on trapped ions using a charge-coupled device (CCD) camera. We discuss extending this measurement and control to larger numbers of qubits through the use of a multi-zone trap array capable of physically transporting and re-arranging ion qubits. Moreover, we propose a new direction for quantum information research through the first confinement of neutral Cadmium atoms and its implications for future work in coherent quantum information transfer and processing.

CHAPTER I

Motivation and Introduction

In this thesis we describe experiments united under the theme of detecting and controlling atomic cadmium, both in its singly-ionized and neutral forms.

Motivation for controlling atomic states comes from both applied and theoretical rationales.

On the "applied" end, quantum state detection and control are prerequisites for performing quantum computation and information processing whether via standard circuit-based approaches [1] or via one-way, measurement-based methods [2, 3]. These applications have drawn interest for their potential to outperform a classical computer in such tasks as fast number factoring [4] and database searching [5]. Moreover, quantum state control is also necessary for performing quantum simulations to controllably model systems with Hamiltonians that are far too complex for classical simulation techniques [6].

However, there is also rich interest in the "fundamental" tests of physical theories that quantum state control enables. From precision metrology [7] to the completeness of quantum mechanics [8, 9, 10] and tests of QED [11], quantum state control serves as a testbed for exploring these basic physical theories.

Atomic cadmium in particular represents a potentially interesting system for im-

plementing quantum state control. Singly-ionized Cd^+ can be trapped and controlled for long periods of time in rf Paul traps with individual ions able to be stored for up to several days [12]. Moreover, when controlling the hyperfine states of odd-isotope ions, the coherence time is long enough to allow for large numbers of coherent operations [1].

After this introduction, Chapter II [13] gives a detailed theoretical description and experimental demonstration of our ability to detect the quantum bit (qubit) state of individual atomic ions. We discuss the important requirement of a multi-qubit measurement capability and the theoretical and technical challenges this entails.

Next, we discuss a trap architecture for reliably controlling many ions in Chapter III, with the goal of achieving full quantum state control over many ions simultaneously. In order to extend our control from individual ions to many qubits requires the ability to trap and manipulate the physical arrangement of multiple atomic ions. We discuss the development and usage of a multi-zone "T" trap consisting of an array of ion traps so that individual ions can be reliably shuttled between physical locations.

Chapter IV moves in a new direction by discussing the theory and experimental implementation of trapping neutral Cd atoms. After first describing the necessary experimental apparatus for confining Cd atoms in a magneto-optical trap (MOT), we examine a computer-based simulation of atomic behavior in the MOT with a particular eye towards modeling trap loss mechanisms which can then be compared with experimental data.

Finally, Chapter V presents conclusions and future work, including possible extensions of this work and some significant questions remaining in this field.

CHAPTER II

Multi-Ion Qubit Detection: Theory and Experiment

2.1 Introduction

Trapped atomic ions represent a promising method for implementing universal quantum computation, but one needs to be able to efficiently and faithfully measure the quantum state of each individual ion in order to view the results of any quantum computation. In this chapter, we discuss the important quantum computer requirement of a multi-qubit measurement capability [13].

State detection is typically accomplished by applying polarized laser light resonant with a cycling transition for one of the qubit states and off-resonant for the other state. The two states are then distinguishable as "bright" and "dark" via this state-dependent fluorescence [14, 15, 16, 17]. Typical schemes collect this fluorescence using fast lenses and detect photons using a standard photon-counting device such as a photo-multiplier tube (PMT) or an avalanche photo-diode (APD). The relatively high detection efficiency of PMTs or APDs aids detection, but for detecting more than one ion their lack of spatial resolution means that certain qubit states are indistinguishable, e.g. one bright ion out of two does not determine a particular ion's state. Distinguishable individual qubit state detection is particularly crucial for tomographic density matrix reconstruction [18, 19], quantum algorithms [20,

21], quantum error correction [22], and cluster state quantum computation [2, 3]. Separating the ions with shuttling [23, 24, 25, 20, 22] or tightly focussing the detection beam [18] can distinguish the qubits, but the additional time necessary for detection, possible decoherence associated with shuttling, and technical difficulties make these schemes less desirable for large numbers of ions.

In this chapter, we discuss the use of an intensified charge-coupled device (CCD) as a photon-counting imager for simultaneously detecting multiple qubit states with high efficiency. We first theoretically model the detection fidelity of qubits stored in $S_{1/2}$ hyperfine states of alkali-like ions, where one of the qubit states has a closed transition to the excited electronic P state manifold (applicable to odd isotopes of Be^+, Mg^+, Zn^+, Cd^+, Hg^+, and Yb^+). We then present data for the detection of several $^{111}Cd^+$ ions using a CCD imager, and discuss technical features and limitations of current CCD technology. We finish with a discussion of future improvements and prospects for integration with scalable quantum computation architectures [13].

2.2 Detection Theory

2.2.1 Basic detection method There are two classes of alkali-like atomic ions that are amenable to high-fidelity $S_{1/2}$ hyperfine-state qubit detection. Ions that do not have a closed transition to the excited electronic P state require shelving of one of the hyperfine qubit states to a low-lying metastable electronic D state (odd isotopes of Ca^+, Sr^+, and Ba^+). The detection efficiencies in this case can be very high; typically this method requires a narrowband laser source for high-fidelity shelving [26, 27] although recent work using rapid adiabatic passage may relax this laser requirement [28]. Alternatively, one can obtain moderate detection efficiency by using coherent population trapping to optically shelve a particular spin state [29].

In contrast, ions that possess a closed transition to the excited electronic P state (odd isotopes of Be^+, Mg^+, Zn^+, Cd^+, Hg^+, and Yb^+) can be detected directly, and will be the focus of this paper. Throughout this paper we assume that the Zeeman splitting is small compared to the hyperfine splittings.

There are two basic schemes for this direct state detection as outlined in figure 2.1. For both methods, the qubit is stored in the hyperfine levels of the $S_{1/2}$ manifold with hyperfine splitting ω_{HFS}. Discussing the general case first (fig. 2.1a), if we write the states in the $|F, m_F\rangle$ basis with I the nuclear spin, the $S_{1/2}\,|I+1/2, I+1/2\rangle \equiv |\mathbf{1}\rangle$ state exhibits a closed "cycling" transition to the $P_{3/2}\,|I+3/2, I+3/2\rangle$ state when resonant σ^+-polarized laser light is applied[1]. If the qubit is in the $|\mathbf{1}\rangle$ state then the resonant laser light induces a large amount of fluorescence. When a portion of these photons are collected and counted on a photon-counting device, a histogram of their distribution follows a Poissonian distribution with a mean number of collected photons that is determined by the laser intensity and application time, the upper-state radiative linewidth γ, and the photon collection efficiency of the detection system. In contrast, when the qubit is in the $S_{1/2}\,|I-1/2, I-1/2\rangle \equiv |\mathbf{0}\rangle$ state the laser radiation is no longer resonant with the transition to any excited state. The nearest allowed transition is to $P_{3/2}\,|I+1/2, I+1/2\rangle$ which is detuned by $\Delta = \omega_{\mathrm{HFS}} - \omega_{\mathrm{HFP}}$, where ω_{HFP} is the hyperfine splitting of the $P_{3/2}$ states, so an ion in the $|\mathbf{0}\rangle$ state scatters virtually no photons. Thus, we can determine the qubit's state with high fidelity by applying σ^+-polarized laser radiation resonant with the cycling transition and counting the number of photons that arrive at the detector.

For ions with isotopes that have nuclear spin $I = 1/2$ (Cd^+, Hg^+, and Yb^+), there is another possible state-dependent fluorescence detection mechanism by coupling to

[1]Equivalently one could use σ^--polarized radiation with appropriate qubit and excited states.

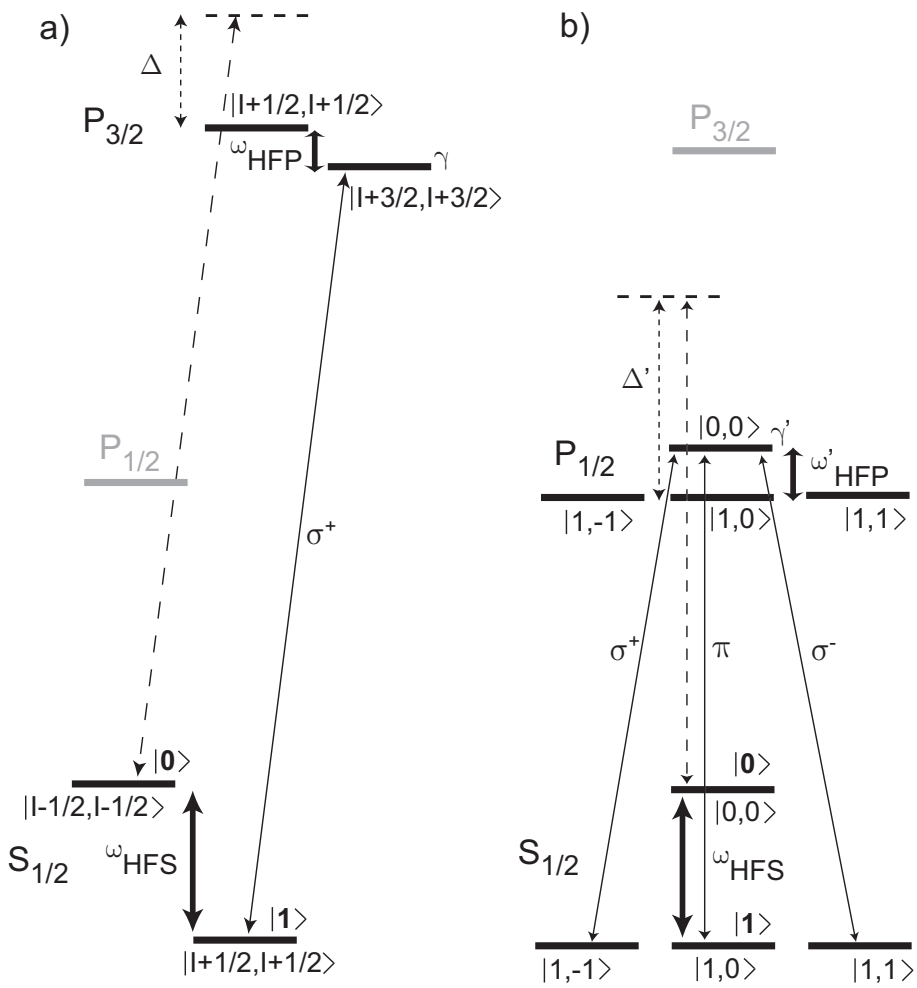

Figure 2.1: Relevant energy levels used in fluorescence detection of qubits. This diagram is applicable for qubits stored in the hyperfine levels of the $S_{1/2}$ ground state of atoms with a single valence electron, with no relevant low-lying excited states below the excited P manifold. Energy levels are labeled by the $|F, m_F\rangle$ quantum numbers of total angular momentum and the energy splittings are not to scale. a) Detection through $P_{3/2}$ level with qubit stored in the $S_{1/2}\,|I+1/2, I+1/2\rangle \equiv |\mathbf{1}\rangle$ and $S_{1/2}\,|I-1/2, I-1/2\rangle \equiv |\mathbf{0}\rangle$ "stretch" hyperfine states, for any nonzero nuclear spin I. By applying σ^+-polarized laser radiation resonant with the $|\mathbf{1}\rangle \rightarrow P_{3/2}\,|I+3/2, I+3/2\rangle$ cycling transition, qubit state $|\mathbf{1}\rangle$ results in strong fluorescence, while qubit state $|\mathbf{0}\rangle$ is nearly dark owing to a detuning of $\Delta = \omega_{\mathrm{HFS}} - \omega_{\mathrm{HFP}} \gg \gamma$ to the nearest resonance, where ω_{HFS} and ω_{HFP} are the hyperfine splittings of the $S_{1/2}$ and $P_{3/2}$ states and γ is the radiative linewidth of the $P_{3/2}$ state. b) Detection through the $P_{1/2}$ level with qubit stored in the $S_{1/2}\,|1, 0\rangle \equiv |\mathbf{1}\rangle$ and $S_{1/2}\,|0, 0\rangle \equiv |\mathbf{0}\rangle$ "clock" hyperfine states for the special case of nuclear spin $I = 1/2$. Here, applying all polarizations of laser radiation resonant with the $|\mathbf{1}\rangle \rightarrow P_{1/2}\,|0, 0\rangle$ transition results in strong fluorescence, while qubit state $|\mathbf{0}\rangle$ is nearly dark owing to a detuning of $\Delta' = \omega_{\mathrm{HFS}} + \omega'_{\mathrm{HFP}} \gg \gamma'$ to the nearest resonance, where ω_{HFS} and ω'_{HFP} are the hyperfine splittings of the $S_{1/2}$ and $P_{1/2}$ states and γ' is the radiative linewidth of the $P_{1/2}$ state.

the $P_{1/2}$ manifold (fig. 2.1b). If we apply all polarizations of laser light (σ^+, π, and σ^-) resonant with the $S_{1/2}\,|F=1\rangle \rightarrow P_{1/2}\,|F=0\rangle$ transition then the only allowed decay from the excited state is back to the $F=1$ levels of $S_{1/2}$ [30], forming a closed cycling transition. If the ion begins in the state $|1,0\rangle \equiv |\mathbf{1}\rangle$, the ion will fluoresce many photons under this laser stimulation and we can collect these photons as above. Conversely, the state $|0,0\rangle \equiv |\mathbf{0}\rangle$ will scatter virtually no photons under this laser light because it is off-resonant from its only allowed transition to the $P_{1/2}\,|F=1\rangle$ levels by $\Delta' = \omega_{\mathrm{HFS}} + \omega'_{\mathrm{HFP}}$, where ω'_{HFP} is the hyperfine splitting of the $P_{1/2}$ levels. Note that to avoid an optically-pumped dark state formed by a coherent superposition of $S_{1/2}\,|1,-1\rangle$, $|1,0\rangle$, and $|1,1\rangle$ it is necessary to modulate the laser polarization or use a magnetic field to induce a well-chosen Zeeman splitting [31].

In the following sections we present a general theory of this state-dependent fluorescence by determining the off-resonant coupling between the qubit states. We quantify these detection errors in order to calculate the fidelity of qubit state detection for various photon detection efficiencies.

2.2.2 Statistics: dark → bright leakage For both the general and the $I = 1/2$ specific detection methods, qubits in the dark state can leak onto the bright transition by off-resonantly coupling to the wrong hyperfine excited level during detection. Rate equations describing this off-resonant pumping yield an exponential probability distribution of remaining in the dark state as a function of time. Once in the bright state, the collected photons from the closed transition obey Poissonian statistics. Therefore, for a qubit initially in the dark state, we expect the distribution of emitted photons to be a convolution of Poissonian and exponential distributions [32, 33], as we now derive.

The probability of leaving the dark state at a time t is given by:

$$f(t)\mathrm{d}t = \frac{1}{\tau_{L1}} e^{-\frac{t}{\tau_{L1}}} \mathrm{d}t \tag{2.1}$$

where τ_{L1} is the average leak time of the dark state onto the closed transition. Also, the average number of collected photons for a qubit that starts dark but is pumped to a bright state at time t is:

$$\lambda(t) = (1 - \frac{t}{\tau_D})\lambda_0 \tag{2.2}$$

where τ_D is the detection time and λ_0 is the mean number of *counted* photons when starting in the bright state.

We want to transform from a probability distribution $f(t)\mathrm{d}t$ to a probability distribution of Poissonian means $g(\lambda)\mathrm{d}\lambda$ so we use eqn. 2.2 to get $t(\lambda)$ and then substitute into eqn. 2.1. This yields the probability of the dark qubit state producing a Poissonian distribution of collected photons with mean λ:

$$g(\lambda)\mathrm{d}\lambda = \begin{cases} \frac{\alpha_1}{\eta} e^{(\lambda-\lambda_0)\alpha_1/\eta}\mathrm{d}\lambda & \lambda > 0 \\ e^{-\alpha_1\lambda_0/\eta} & \lambda = 0 \end{cases} \tag{2.3}$$

where $\eta = \eta_D \frac{\mathrm{d}\Omega}{4\pi} T$ is the total photon collection efficiency determined by the detector efficiency (η_D), the solid angle of collection ($\frac{\mathrm{d}\Omega}{4\pi}$), and the optical transmission from the ion to the detector (T); $\alpha_1 \equiv \frac{\tau_D \eta}{\tau_{L1}\lambda_0}$ is the leak probability per *emitted* photon; and the $\lambda = 0$ discontinuity is necessary to account for the fraction that do not leave the dark state (and hence are not described by Poissonian statistics).

Therefore, the probability of detecting n photons when starting in the dark state is the convolution of $g(\lambda)$ with the Poissonian distribution $P(n|\lambda) = \frac{e^{-\lambda}\lambda^n}{n!}$:

$$p_{\mathrm{dark}}(n) = \delta_n e^{-\alpha_1\lambda_0/\eta} + \int_{\epsilon}^{\lambda_0} \frac{e^{-\lambda}\lambda^n}{n!} \frac{\alpha_1}{\eta} e^{(\lambda-\lambda_0)\alpha_1/\eta}\mathrm{d}\lambda \tag{2.4}$$

with δ_n the Kronecker delta function and $\epsilon \to 0$. Re-writing in terms of the incomplete Gamma function we obtain:

$$p_{\text{dark}}(n) = e^{-\alpha_1\lambda_0/\eta}\left[\delta_n + \frac{\alpha_1/\eta}{(1-\alpha_1/\eta)^{n+1}}\mathcal{P}(n+1,(1-\alpha_1/\eta)\lambda_0)\right] \tag{2.5}$$

where $\mathcal{P}(a,x) \equiv \frac{1}{(a-1)!}\int_0^x e^{-y}y^{a-1}\mathrm{d}y$ is the standard definition of the incomplete Gamma function normalized such that $\mathcal{P}(a,\infty) = 1$.

Figure 2.2a shows this probability distribution for various values of the leakage parameter, α_1. In sec. 2.2.4, we will calculate physical values of α_1 and λ_0 from the atomic parameters.

2.2.3 Statistics: bright → dark leakage Similarly, the bright state can be optically pumped into the dark state by off-resonant coupling to the wrong excited hyperfine level. When using the $P_{3/2}$ manifold for detection this coupling can only occur for imperfect laser polarizations, while for the specialized $I = 1/2$, $P_{1/2}$ case this off-resonant coupling is always present (since all laser polarizations are applied). As before, the overall photon probability distribution will be a convolution of Poissonian and exponential distributions, but now reversed: after some time scattering photons on the closed transition the qubit is pumped into the dark state and emits no more photons (neglecting the 2nd order effect of then re-pumping from the dark state back to the bright state). If we define the leak probability per emitted photon $\alpha_2 \equiv \frac{\tau_D\eta}{\tau_{L2}\lambda_0}$ where τ_{L2} is the average leak time from the cycling transition into the dark state, then with similar statistics as before, the probability of detecting n photons when starting in the bright state is:

$$p_{\text{bright}}(n) = \frac{e^{-(1+\alpha_2/\eta)\lambda_0}\lambda_0^n}{n!} + \frac{\alpha_2/\eta}{(1+\alpha_2/\eta)^{n+1}}\mathcal{P}(n+1,(1+\alpha_2/\eta)\lambda_0) \tag{2.6}$$

where the first term is the Poissonian distribution from never leaving the closed transition and the second term is the smearing of the distribution from pumping to

the dark state (note that $\alpha_1 \neq \alpha_2$). This distribution is shown in figure 2.2b for varying values of α_2.

One can further separate the dark and bright distributions by using ancilla qubits and entangling gates before measurement [34]. For ions with large leak probabilities α_1 or α_2 this technique may be useful because it can increase qubit detection fidelity to as high as the entangling gate fidelity.

2.2.4 Calculating the atomic parameters

General case using $P_{3/2}$

If we assume a detuning δ of the detection beam from the cycling transition resonance then for ideal σ^+-polarized laser radiation the mean number of photons *detected* from a qubit in $|\mathbf{1}\rangle$ is:

$$\lambda_0 = \tau_D \eta \frac{s\frac{\gamma}{2}}{1 + s + \left(\frac{2\delta}{\gamma}\right)^2} \tag{2.7}$$

where τ_D is the detection time; η is the *total* end-to-end efficiency of photon detection; γ is the radiative linewidth of the $P_{3/2}$ state; and $s = I/I_{\text{sat}}$ is the laser-ion saturation parameter.

Next we can calculate α_1, the probability per emitted photon of leakage from the dark state into the bright state. The dark state can off-resonantly couple to the $P_{3/2}\,|I+1/2, I+1/2\rangle$ level with probability that goes as: $\sim s\left(\frac{\gamma}{2\Delta_1}\right)^2$, where $\Delta_1 = \omega_{\text{HFS}} - \omega_{\text{HFP}}$ is the $S_{1/2}$ hyperfine splitting minus the $P_{3/2}$ hyperfine splitting between $|I+3/2, I+3/2\rangle$ and $|I+1/2, I+1/2\rangle$. We also need to take into account the branching ratio, $\mathbf{M_1}$, to determine the transition rate between the dark state and the cycling transition. Thus, we can write the value of α_1 as:

$$\alpha_1 = \mathbf{M_1}\left[1 + s + \left(\frac{2\delta}{\gamma}\right)^2\right]\left(\frac{\gamma}{2\Delta_1}\right)^2. \tag{2.8}$$

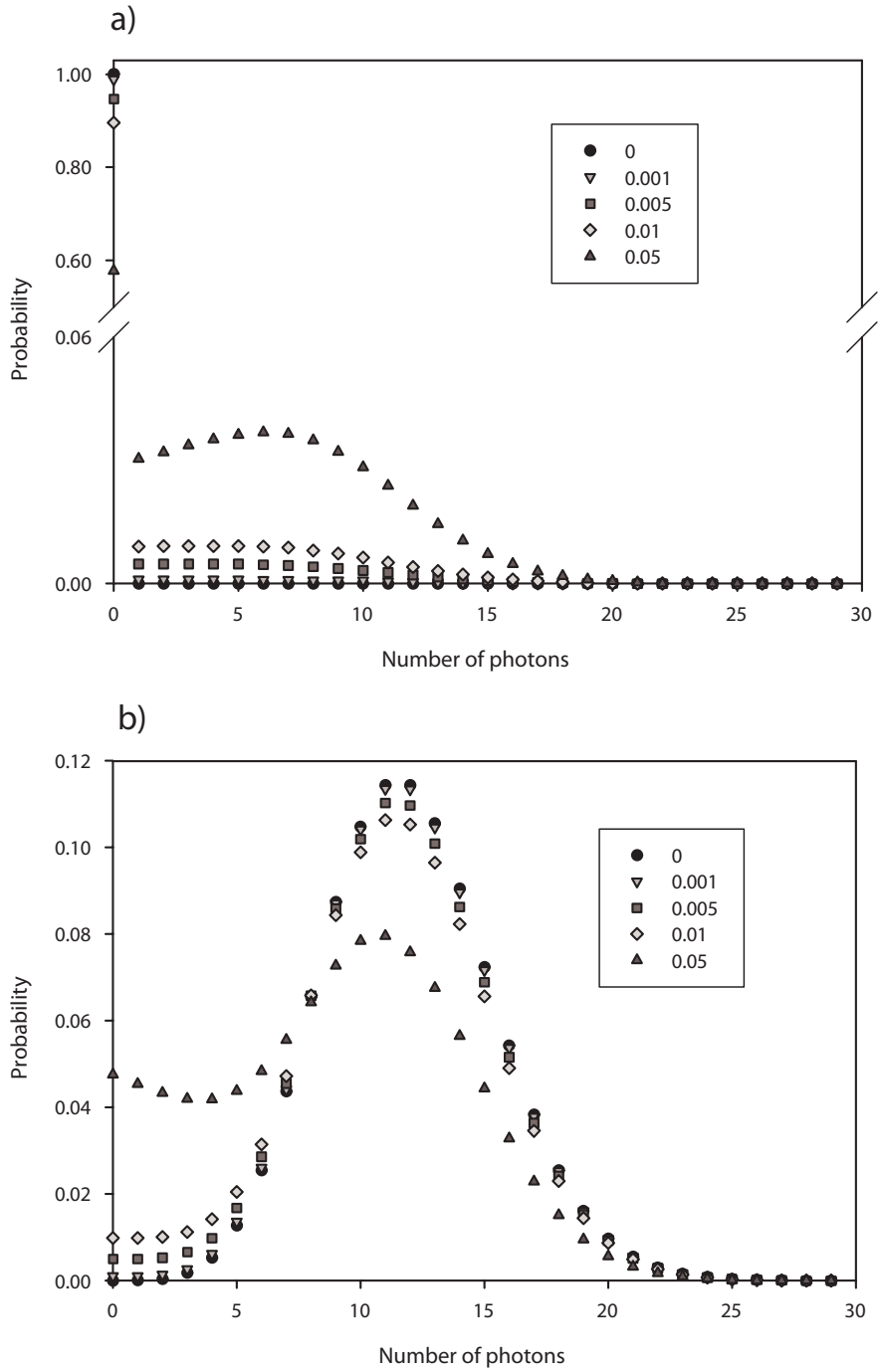

Figure 2.2: Theoretical "bright" and "dark" histograms with varying leakage parameters. These photon count histograms are for ions that start in: a) the nominally "dark" $|\mathbf{0}\rangle$ state; and b) the nominally "bright" $|\mathbf{1}\rangle$ state. Both plots use $\lambda_0 = 12$ with varying values of: a) α_1/η (the leakage probability from the dark state to the bright state per *detected* photon) and b) α_2/η (the leakage probability from the bright state to the dark state per *detected* photon).

We can calculate the braching ratio, $\mathbf{M_1}$, by considering off-resonant coupling between the dark state ($|I-1/2, I-1/2\rangle$) and the state $P_{3/2}\,|I+1/2, I+1/2\rangle$. This state can then decay into the bright manifold ground states $|I+1/2, I\pm 1/2\rangle$. The generalized formula can be written as:

$$\begin{aligned}\mathbf{M_1} &= C(I-1/2, I+1/2; I-1/2, I+1/2) \sum_{i=I-1/2}^{I+1/2} C(I+1/2, I+1/2; I+1/2, i) \\ &= \frac{4I(3+2I)}{9(1+2I)^2}. \end{aligned} \tag{2.9}$$

where we have used that $C(F, F'; f, f')$ is the square of the Clebsch-Gordon coefficient between two states $F \to F'$ and $m_F = f \to f'$ given by [35]:

$$\begin{aligned} C(F, F'; f, f') = {} & [(2J+1)(2J'+1)(2F+1)(2F'+1)] \\ & \times \left[\begin{Bmatrix} L' & J' & S \\ J & L & 1 \end{Bmatrix} \begin{Bmatrix} J' & F' & I \\ F & J & 1 \end{Bmatrix} \begin{pmatrix} F & 1 & F' \\ f & q & -f' \end{pmatrix} \right]^2 \end{aligned} \tag{2.10}$$

where $\{\}$ is the 6-J symbol, $()$ is the 3-J symbol with polarization number q, and there is an implied normalization constant such that the cycling transition strength is 1.

Similarly, we can calculate α_2, the probability per emitted photon of leakage from the bright state into the dark state. Note that there are two leakage paths out of the bright state: via coupling to the $P_{3/2}\,|I+1/2, I+1/2\rangle$ state (due to π-polarized laser light) or to the $P_{3/2}\,|I+1/2, I-1/2\rangle$ state (due to σ^--polarized radiation). These two paths yield a leakage probability:

$$\alpha_2 = \left[1 + s + \left(\frac{2\delta}{\gamma}\right)^2\right] \left(\frac{\gamma}{2\Delta_2}\right)^2 \frac{\mathbf{M_{2\pi}} P_\pi + \mathbf{M_{2-}} P_-}{1-(P_\pi + P_-)} \tag{2.11}$$

where $\Delta_2 = \omega_{\mathrm{HFP}}$ is the hyperfine splitting of the $P_{3/2}$ levels, P_π (P_-) is the fraction of π (σ^-)-polarized laser power, and $\mathbf{M_{2\pi}}$ ($\mathbf{M_{2-}}$) is the dipole branching ratio for π

(σ^-)-polarized light impurity. These branching ratios are given by:

$$\begin{aligned}\mathbf{M_{2\pi}} &= C(I+1/2, I+1/2; I+1/2, I+1/2) \\ &\times C(I-1/2, I+1/2; I-1/2, I+1/2) \\ &= \frac{4I}{9+18I}\end{aligned} \tag{2.12}$$

and

$$\begin{aligned}\mathbf{M_{2-}} &= C(I+1/2, I+1/2; I+1/2, I-1/2) \\ &\times C(I-1/2, I+1/2; I-1/2, I-1/2) \\ &= \frac{16I}{9(1+2I)^3}.\end{aligned} \tag{2.13}$$

$I = 1/2$ **case using** $P_{1/2}$

For the special case of detecting the qubit state via the $P_{1/2}$ manifold, we need to make some small adjustments to our calculations. Assuming that the laser power is split roughly equally between the 3 polarizations, the mean number of collected, scattered photons when starting in one of the bright, $F = 1$ states is:

$$\lambda_0' = \tau_D \eta \frac{s\frac{\gamma'}{2}}{1+s+\left(\frac{2\delta}{\gamma'}\right)^2} \tag{2.14}$$

where γ' is the radiative linewidth of the $P_{1/2}$ state.

For the dark state leakage per emitted photon, α_1', we simply have a new relevant detuning Δ_1' and branching ratio $\mathbf{M_1'}$:

$$\alpha_1' = \mathbf{M_1'}\left[1+s+\left(\frac{2\delta}{\gamma'}\right)^2\right]\left(\frac{\gamma'}{2\Delta_1'}\right)^2. \tag{2.15}$$

where the relevant detuning is now $\Delta_1' = \omega_{\mathrm{HFS}} + \omega_{\mathrm{HFP}}'$, namely the $S_{1/2}$ state hyperfine splitting plus the $P_{1/2}$ state hyperfine splitting. For the $I = 1/2$ ions, all allowed dipole transitions have relative strength of 1/3, so the dark state leakage branching ratio is: $\mathbf{M_1'} = 1/3 \times (1/3 + 1/3) = 2/9$.

Also, the bright state can leak into the dark state via off-resonant coupling to one of the $P_{1/2}$, $F = 1$ states with probability per emitted photon of:

$$\alpha_2' = \mathbf{M_2'} \left[1 + s + \left(\frac{2\delta}{\gamma'} \right)^2 \right] \left(\frac{\gamma'}{2\Delta_2'} \right)^2 \tag{2.16}$$

where $\Delta_2' = \omega_{\mathrm{HFP}}'$, the hyperfine splitting of the $P_{1/2}$ state, and $\mathbf{M_2'} = (1/3 + 1/3) \times 1/3 = 2/9$.

2.3 Comparison of Theory with Experiment

We now compare the above model to experimental data for $^{111}\mathrm{Cd}^+$ qubits using a PMT for photon detection. For this calculation and experiment we use the general detection technique that couples to the $P_{3/2}$ levels.

In the experiment, individual $^{111}\mathrm{Cd}^+$ ions ($I = 1/2$) are produced through photo-ionization of neutral Cd and then confined in a linear RF Paul trap with controllable axial frequency $\omega_z/2\pi = 0.5 - 2.5$ MHz [36]. The qubit is stored in the first-order magnetic field-insensitive "clock" states: $|0,0\rangle \equiv |\mathbf{0}\rangle$ and $|1,0\rangle \equiv |\mathbf{1}\rangle$.

In $^{111}\mathrm{Cd}^+$, for σ^+-polarized laser light the large hyperfine splitting of the $P_{3/2}$ states ensures that population in the $S_{1/2}\,|1,0\rangle$ state is optically pumped to the $S_{1/2}\,|1,1\rangle$ with high probability so the $P_{3/2}$ detection theory given in sec. 2.2.4 will apply well to this case (corrections are given in sec. 2.4.1). For $^{111}\mathrm{Cd}^+$, the relevant energy splittings are: $\gamma/2\pi = 60.1$ MHz, $\Delta_1/2\pi = 13.904$ GHz, $\Delta_2/2\pi = 626$ MHz [37, 38, 39] and we choose the laser wavelength such that the detuning $\delta \approx 0$ (figure 2.3). The branching ratios are calculated from eqns. 2.9, 2.12, and 2.13: $\mathbf{M_1} = 2/9$ and $\mathbf{M_{2\pi}} = \mathbf{M_{2-}} = 1/9$. Because $\mathbf{M_{2\pi}} = \mathbf{M_{2-}}$, the π- and σ^--polarized components can be treated together and we can define an overall laser power impurity $P_{impure} \equiv P_\pi + P_-$. Experimentally, we know the detection time, τ_D, and we can leave η, P_{impure}, and s as free parameters to be determined by the fit to experimen-

tal data (although in principle one could independently measure these parameters). Figure 2.4 shows the good agreement between theory and experiment.

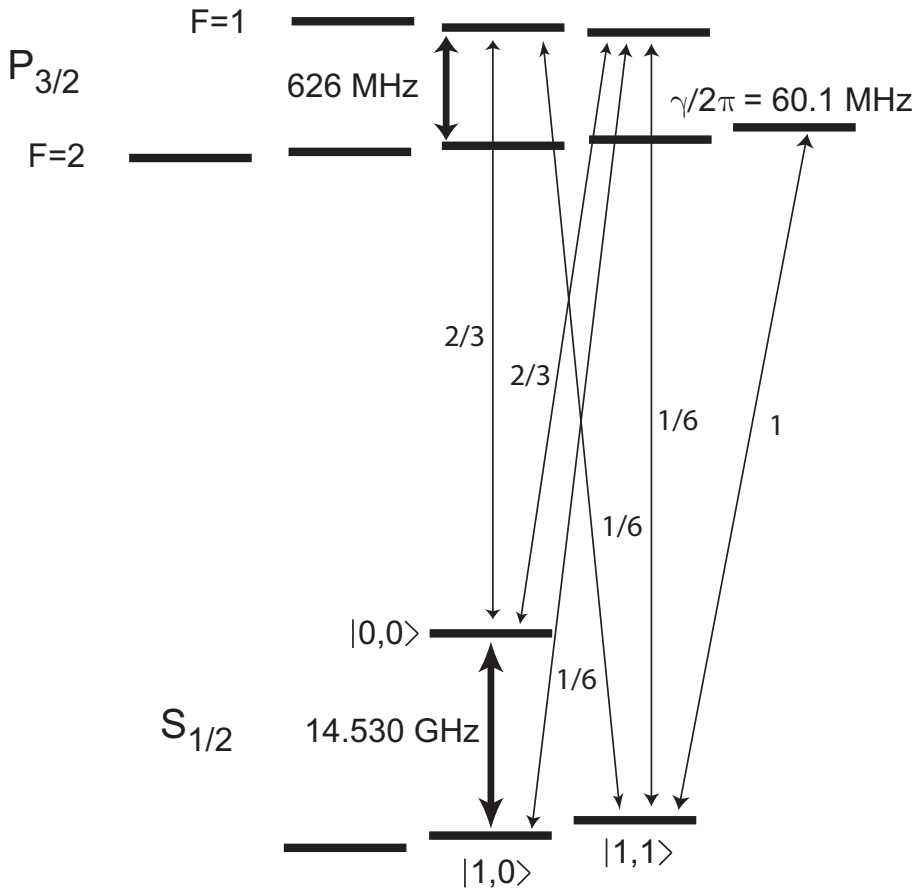

Figure 2.3: Relevant energy levels and relative dipole transition strengths for state detection of $^{111}Cd^{+}$. Note that the Zeeman splitting (< 10 MHz) is small compared to the hyperfine splittings.

2.4 Theoretical Limit of Detection Fidelity

2.4.1 Detection with $P_{3/2}$ levels To determine the theoretical limit of detection fidelity for $^{111}Cd^{+}$ using the $P_{3/2}$ levels we choose the most ideal conditions: small laser detuning from resonance ($\delta \to 0$) and perfect detection beam polarization so the bright state histogram is a true Poissonian ($P_{impure} = 0$ which means $\alpha_2 = 0$). Moreover, with perfect polarization we can lower the laser intensity ($s \ll 1$) to eliminate power-broadening while increasing τ_D to maintain a sufficiently bright

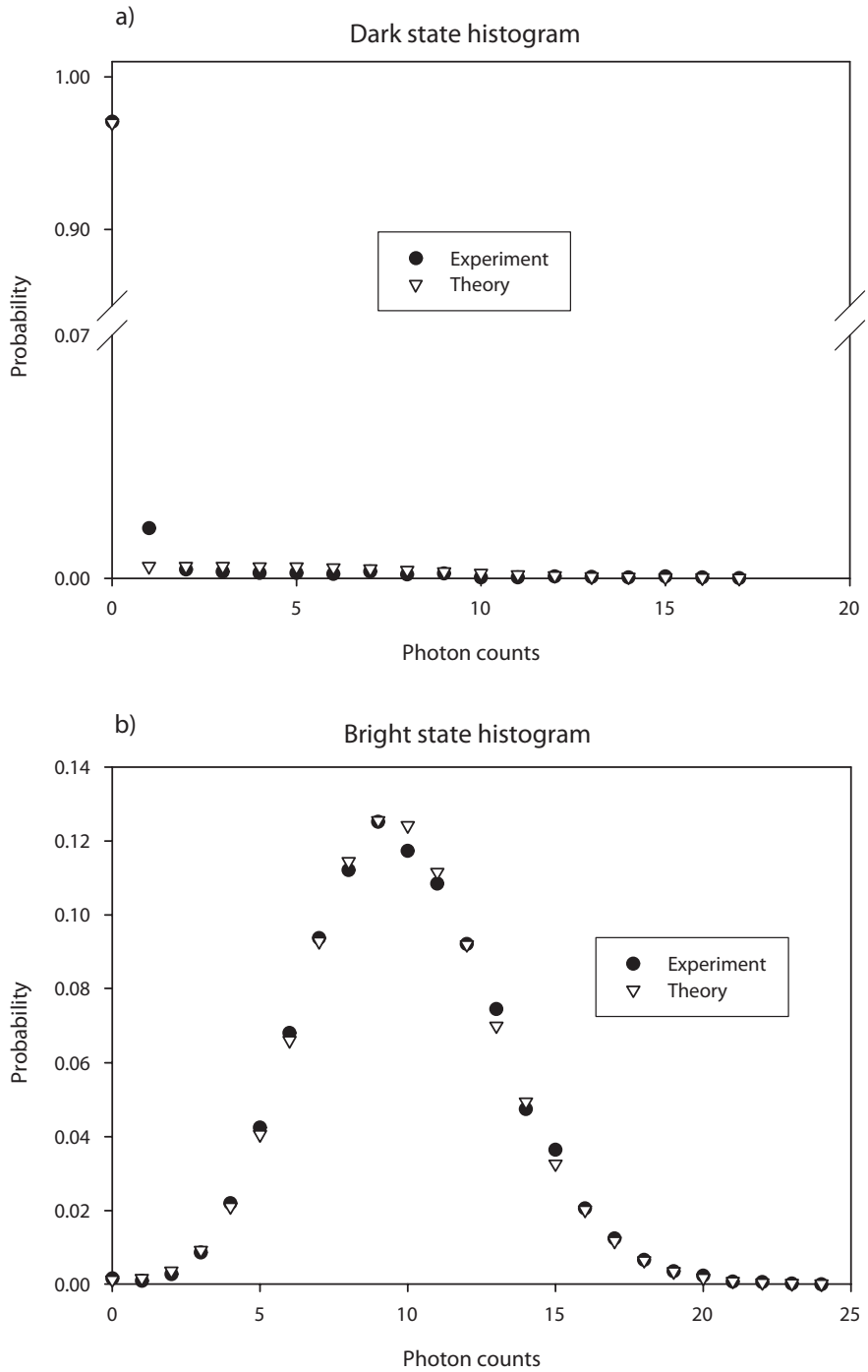

Figure 2.4: Fit to experimental histograms for $^{111}Cd^{+}$. Detection histograms using a PMT and the $P_{3/2}$ detection scheme for a single $^{111}Cd^{+}$ ion prepared in: a) $|0,0\rangle \equiv |\mathbf{0}\rangle$ dark state; and b) $|1,0\rangle \equiv |\mathbf{1}\rangle$ bright state. For the data shown, each state is prepared and then measured 20,000 times. Fit is to theory from text (eqn. 2.5 and eqn. 2.6, respectively) with parameters: $\tau_D = 150\mu$s, $\eta = 1.4 \times 10^{-3}$, $P_{\text{impure}} = 1.5 \times 10^{-3}$, and $s = 0.25$. Note that for the experimental data in a), the $n = 1$ bin includes background light scatter that the model does not include.

"bright" state.

Using a discriminator at photon level d, detection fidelity of the bright state is the probability that the ion scatters *more* than d photons while for the dark state it is the probability that it scatters d or fewer photons. The overall qubit detection efficiency is the average of these two numbers and it is typically maximized for the two fidelities being equal. Thus, the optimal qubit detection fidelity, F, is:

$$F = \sum_{n=0}^{d} p_{\text{dark}}(n) = 1 - \sum_{n=0}^{d} p_{\text{bright}}(n) \tag{2.17}$$

with $\lambda_0 = s\tau_D\eta\frac{\gamma}{2}$ and $\alpha_1 = \mathbf{M_1}(\frac{\gamma}{2\Delta_1})^2$ given our assumptions mentioned above.

To calculate the detection fidelity, we find $\alpha_1 = 1.0 \times 10^{-6}$ for $^{111}\text{Cd}^+$. Then we can choose the optimal λ_0 for discrimination by controlling the effective light level on the ion (adjusting the product $s\tau_D$). For our current experimental value of $\eta \approx 0.001$ the optimum light level yields $\lambda_0 = 5.6$ and, using the discriminator level $d = 0$, we obtain a qubit detection fidelity of $F = 99.5\%$. In practice, the optimal light level is slightly higher to aid in discriminating the background laser scatter from the bright qubit fluorescence.

We can obtain a useful approximate analytic result for the theoretical qubit fidelity as a function of detector collection efficiency by assuming a discriminator level $d = 0$. The optimal situation is when the fidelity of bright state detection and dark state detection are equal: $F = e^{-\alpha_1\lambda_0/\eta} = 1 - e^{-\lambda_0}$ (eqn. 2.17). The term $\alpha_1\lambda_0/\eta$ is typically small so we Taylor expand and then take the natural logarithm of both sides to find:

$$\lambda_0 + \ln\lambda_0 \approx -\ln(\alpha_1/\eta) \tag{2.18}$$

We wish to obtain a closed form solution for λ_0 as a function of α_1 and η since α_1 depends only on atomic parameters. Therefore, for the typical case of optimal

$\lambda_0 \sim 5 - 15$ it is reasonable to further assume that $\ln \lambda_0 \ll \lambda_0$ so that the ideal light level is approximately $\lambda_0 \approx -\ln(\alpha_1/\eta) = \ln(\eta/\alpha_1)$ and the approximate fidelity is:

$$F_{\text{approx}} \approx 1 - \frac{\alpha_1}{\eta} \ln(\frac{\eta}{\alpha_1}). \tag{2.19}$$

This result gives an accurate scaling of the fidelity as a function of detector collection efficiency (figure 2.5).

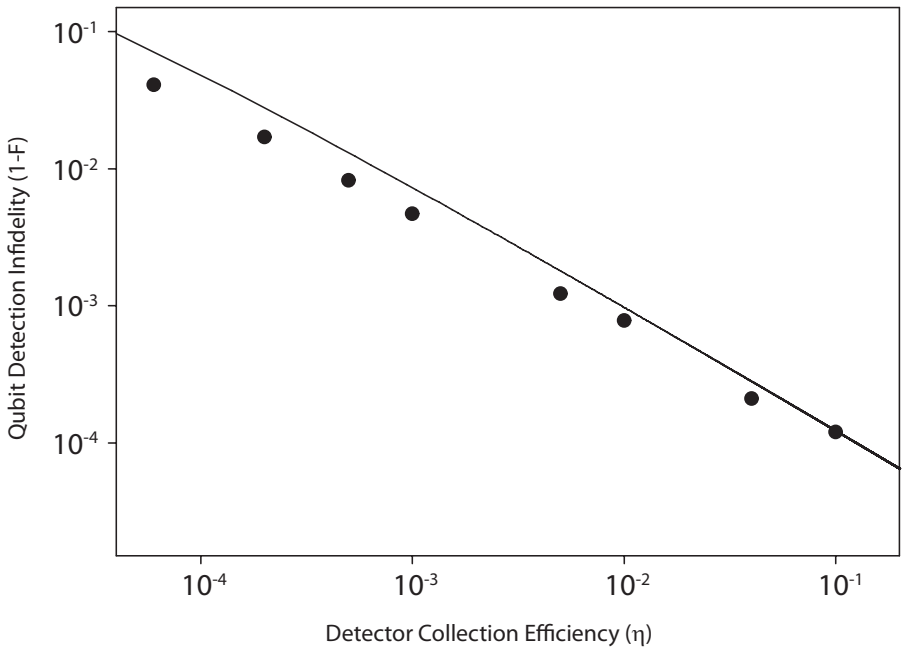

Figure 2.5: Theoretical prediction of detection infidelity (1-F) using the $P_{3/2}$ detection scheme for $^{111}\text{Cd}^+$ as a function of total detector collection efficiency (η). Filled circles are numerically calculated using eqn. 2.17 with iterations to find the optimal light level and detection time for each η; solid curve uses the approximate analytic result of eqn. 2.19.

In an ideal case, we could use a cavity to surround the ion [40] to increase the solid angle of light collected and a detector with very high quantum efficiency. This might produce a photon collection efficiency as high as $\sim 30\%$ which, using eqn. 2.17, would yield a fidelity: $F_{\text{ideal}} = 99.997\%$.

At this point we hit a fundamental limitation of fluorescence state detection when using the $P_{3/2}$ levels and a qubit stored in the clock states: even with perfect polarization the $|1,0\rangle \equiv |\mathbf{1}\rangle$ state can off-resonantly couple to the $|0,0\rangle \equiv |\mathbf{0}\rangle$ dark state

before ever reaching the cycling transition. This coupling is unaffected by any external parameters and is a property of the atomic structure only. Given this inherent error, the maximum fidelity of direct clock state qubit detection is given by:

$$F_{\max} = 1 - P_{|1,0\rangle \to \text{dark}} = 1 - \frac{4}{9}\left(\frac{\gamma}{2\omega_{\text{HFP}}}\right)^2. \tag{2.20}$$

Here, the pre-factor of 4/9 comes from the Clebsch-Gordon coeffecients and the ensuing probability ratio of never reaching the cycling transition even when starting in the "bright" $|1,0\rangle$ state. To work this out for Cd^+, consider that for starting in the $|1,0\rangle$ state the path to reach the $|1,1\rangle$ state involves a transition up and down through the $|2,1\rangle$ upper state which involves two transitions each of probability 1/2. But the electron can also reach the cycling transition even if from the upper $|2,1\rangle$ state it decays back to the starting $|1,0\rangle$ state and then undertakes the up/down transition we described before. Therefore, the total probability of reaching the cycling transition from the initial $|1,0\rangle$ state is given by the converging infinite series:

$$\frac{1}{2}\cdot\frac{1}{2} + \frac{1}{2}\cdot\frac{1}{2}\cdot\frac{1}{2}\cdot\frac{1}{2} + \ldots = \frac{1}{4}\sum_{k=0}^{\infty}\left(\frac{1}{4}\right)^k = \frac{1}{3}. \tag{2.21}$$

Similarly, if we examine the path for starting in the $|1,0\rangle$ state and reaching the dark $|0,0\rangle$ state we see that it involves a transition through the upper $|1,1\rangle$ state with probabilities up/down of 1/6 and 2/3, respectively. Again, it is possible for the electron to initially decay back to the starting state and yet be excited back through the upper $|1,1\rangle$ state into dark state. The dominant probability is for the initial excitation to be through the $|2,1\rangle$ upper state and then back which leads to the inifinite probability series:

$$\frac{1}{6}\cdot\frac{2}{3} + \frac{1}{2}\cdot\frac{1}{2}\cdot\frac{1}{6}\cdot\frac{2}{3} + \ldots = \frac{1}{9}\sum_{k=0}^{\infty}\left(\frac{1}{4}\right)^k = \frac{4}{27}. \tag{2.22}$$

We then take the ratio of eqns. 2.22 and 2.21 and incorporate the atomic detuning factor to reach the result of eqn. 2.20.

For ions where the $P_{3/2}$ hyperfine splitting is not much larger than the linewidth, the "bright" clock state is not actually very bright because it couples to the dark manifold so easily. Direct fluorescence state detection of clock states is basically impractical for these ions, but there are a number of schemes to improve detection fidelity including using Raman transitions to shelve one of the qubit states in a more off-resonant state (with the detection fidelity now possibly limited by the Raman π-pulse fidelity) and using large magnetic fields to make 1st-order insensitive states with $m_F \neq 0$ [41]. For $^{111}\mathrm{Cd}^+$, $\omega_{\mathrm{HFP}} \gg \gamma/2$, so direct clock state detection yields $F_{\max} = 99.90\%$. Reaching this limit requires a high quantum efficiency detector (see eqn. 2.19), a subject we address in sec. 5.2.1.

2.4.2 Detection with $P_{1/2}$ levels The theoretical limit on detection fidelity when coupling to the $P_{1/2}$ levels is the leakage from one of the bright states into the dark state. With no laser detuning ($\delta \to 0$) and low light level ($s \ll 1$), the relevant parameters become: $\lambda_0' = s\tau_D\eta\frac{\gamma'}{2}$, $\alpha_1' = \frac{2}{9}\left(\frac{\gamma'}{2\Delta_1'}\right)^2$, and $\alpha_2' = \frac{2}{9}\left(\frac{\gamma'}{2\Delta_2'}\right)^2$. Note that the factors of 2/9 that appear in α_1' and α_2' are calculated from $\mathbf{M_1'}$ and $\mathbf{M_2'}$ from sec. 2.2.4. It is always true that $\Delta_1' > \Delta_2'$, so $\alpha_2' > \alpha_1'$ which means that there is always more leakage from the bright state into the dark state than vice versa. Table 2.1 provides the relevant energy splittings for $^{111}\mathrm{Cd}^+$, $^{171}\mathrm{Yb}^+$, and $^{199}\mathrm{Hg}^+$ and the calculated detection fidelity for given values of η, the detector collection efficiency. From the table we can see that for $^{111}\mathrm{Cd}^+$ the advantage of using the $P_{1/2}$ detection scheme instead of the $P_{3/2}$ scheme is only realized for large values of η. Also, note that the fidelity for detecting the qubit state in $^{171}\mathrm{Yb}^+$ is slightly more complicated because there is an allowed decay from the excited $P_{1/2}$ state to a low-lying $D_{3/2}$ state which can be re-pumped to the $S_{1/2}$ level via the $[3/2]_{1/2}$ level [42]. This repumping step is identical to the standard detection step, but its infidelity can be

ignored because the off-resonant coupling is much smaller than for the $P_{1/2}$ detection step due to the energy splittings: $\gamma_{[3/2]}/2\pi = 9.5$ MHz, $\Delta_{\mathrm{HFD}}/2\pi = 0.86$ GHz, $\Delta_{\mathrm{HF}[3/2]}/2\pi = 2.5$ GHz, and $\lambda = 935.2$ nm. A more important modification is that the repumping step takes additional time ($\sim 1/\gamma_{[3/2]}$) so that the number of detectable scattered photons on the $S_{1/2} \rightarrow P_{1/2}$ is reduced by a factor of $\sim 1/3$ while the error probabilities remain the same [43].

Table 2.1: Energy splitting parameters and detection fidelities for $I = 1/2$, $P_{1/2}$ detection scheme. Here we show splittings for $^{111}\mathrm{Cd}^+$ [37, 38], $^{171}\mathrm{Yb}^+$ [44], and $^{199}\mathrm{Hg}^+$ [45] with detection fidelities calculated using eqn. 2.6 for varying detector collection efficiency η.

	$^{111}\mathrm{Cd}^+$	$^{171}\mathrm{Yb}^+$	$^{199}\mathrm{Hg}^+$
$\lambda(S_{1/2} \rightarrow P_{1/2})$ (nm)	226.5	369.5	194
$\gamma'/2\pi$ (MHz)	50.5	23	70
$\Delta_{\mathrm{HFS}}/2\pi$ (GHz)	14.530	12.6	40.5
$\Delta'_{\mathrm{HFP}}/2\pi$ (GHz)	2	2.1	6.9
$\eta = 0.001$	$F = 96.7\%$	$F = 99.33\%$	$F = 99.43\%$
$\eta = 0.01$	$F = 99.65\%$	$F = 99.93\%$	$F = 99.943\%$
$\eta = 0.3$	$F = 99.988\%$	$F = 99.998\%$	$F = 99.998\%$

2.5 Individual Ion Detection Using a CCD

2.5.1 CCD technical overview To benefit from the spatial resolution of a CCD one must typically use an intensified CCD to obtain a signal that is much larger than the CCD readout noise (eqn. 2.23)[2]. In an intensified CCD, single photons incident on the front-screen photocathode produce electrons that are accelerated across a multichannel plate to start a localized electron avalanche that impacts a phosphor screen (figure 2.6). Negative (positive) biasing of the photocathode relative to the multichannel plate produces significant (no) electron acceleration; this differential effect allows for rapid gating of the intensifier and reduces background counts. Visible wavelength photons emitted from the phosphor are then coupled (via lenses or fiber optics) to a standard CCD that converts the photons to charge for readout. The

[2]Recent advances in electron-multiplying CCD (EMCCD) architectures allow for single-photon detection at high readout speeds with low noise (although with no gating capability) [46]. The following discussion, in particular eqn. 2.23, is equally valid for EMCCDs by using the appropriate gain and quantum efficiency.

charge on each pixel of the CCD is then measured with the value proportional to the incident light intensity. A computer PCI board converts the analog voltage signal for each pixel to a digital integer for computer processing.

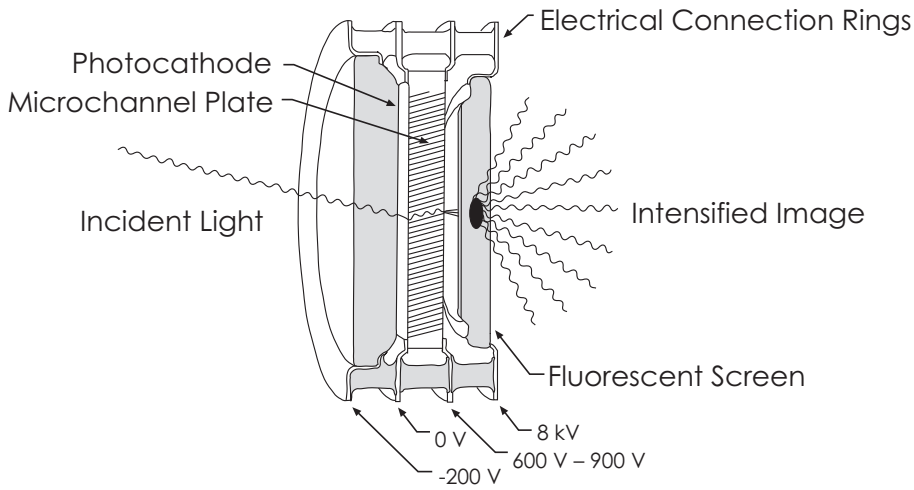

Figure 2.6: Schematic diagram of an intensified CCD camera imaging tube. Incident photons impact the photocathode where they are converted to electrons and accelerated across the multichannel plate. These accelerated electrons strike the phosphor screen and produce visible photons that are coupled into fiber optics and fed onto a standard CCD for readout. Diagram used with permission of Princeton Instruments / Acton.

Technical noise considerations dictate the important CCD characteristic of readout speed. For a qubit in the bright state, the average number of electrons produced at the photocathode by photons incident on the detector during detection is: $\lambda_0 = n_{ion}\eta_D T \mathrm{d}\Omega/4\pi$ where n_{ion} is the number of photons emitted by the ion, η_D is the quantum efficiency of photon to electron conversion, T is the optical transmission between the ion and the detector, and $\frac{\mathrm{d}\Omega}{4\pi}$ is the solid angle of light collection. The remaining stages of electron intensification, conversion to photons, and then photon-induced charge production can be summarized by a gain factor g so that the CCD rms shot noise will be: $g\sqrt{\lambda_0}$. To readout the charge on a pixel, the CCD controller must first clear the charge accumulated during the previous pixel readout. The imperfect repeatability of this process will induce some noise on the signal,

with faster readout speeds leading to less perfect charge cleaning and therefore more noise. This rms noise per readout, r, is uncorrelated to the shot noise so the two noise sources add in quadrature to produce a total noise: $\sqrt{g^2\lambda_0 + (kr)^2}$ where k is the total number of pixels readout. Therefore, the total signal-to-noise ratio (SNR) becomes:

$$\mathrm{SNR} = \frac{g\lambda_0}{\sqrt{g^2\lambda_0 + (kr)^2}} = \frac{\lambda_0}{\sqrt{\lambda_0 + (\frac{kr}{g})^2}}. \tag{2.23}$$

Many CCDs allow on-chip binning of multiple pixel charges together before readout. This on-chip binning increases readout speed and decreases readout noise (because less pixels are readout) at the expense of decreasing spatial resolution (although in principle resolutions above one pixel per ion are unnecessary for distinguishing between the bright and dark states). If $\sqrt{\lambda_0} \ll kr/g$ then the signal is readout noise limited and SNR $\approx \frac{g\lambda_0}{kr}$, so the SNR will improve linearly with the number of pixels binned. For timescales typical of an ion fluorescence experiment, $kr \approx 10$ and so using an intensifier with $g \gg 1$ allows one to use the gain to overwhelm the readout noise. In this shot noise limited regime, the signal-to-noise ratio becomes SNR $\approx \sqrt{\lambda_0}$.

2.5.2 CCD experimental usage For efficient experimental detection we use a 28×28 pixel box on-chip binned 4×4 such that there is an effective box size of 7×7 "super"-pixels. This box size was chosen to match the imager-magnified ion-ion spacing in a trap with $\omega_z/2\pi = 2.0$ MHz so that each ion would be centered in its box with no overlap of boxes; the 4×4 binning improves readout speed yet still offers enough imaging resolution to provide real-time monitoring of ion/imaging system drifts. The detection signal is formed from the integrated electron counts of these 49 pixels minus the constant offset due to the non-zero readout charge maintained on each CCD pixel. Note that this offset is *not* the same as the negligible CCD dark counts

that are caused by inadvertent electron transfer to the back-screen due to thermal effects. We are able to significantly suppress this thermal effect by cooling the CCD.

When histogrammed, the integrated counts for n incident photons show a distribution because multiple electrons and photons are produced for each incident photon with a mean number of integrated counts for this box size of ~ 100 integrated counts per incident photon. Experimentally, the optimal discrimination level is chosen by equalizing the fraction of misidentified states, i.e. choosing a discrimination level such that an equal fraction of $|1,0\rangle \equiv |\mathbf{1}\rangle$ is misidentified as "dark" and $|0,0\rangle \equiv |\mathbf{0}\rangle$ is mislabeled as "bright". Using this optimal discriminator, the efficiency of detecting a single ion's quantum state is $> 99.4\%$ with the lower detection fidelity attributable to the CCD's smaller effective light collection angle (the PMT counts all the incident light while the CCD only uses counts inside the ion pixel box).

2.6 Multiple Ion Detection Using a CCD

2.6.1 Experimental Implementation Of more practical interest than single-ion detection is the ability to detect multiple ion quantum states simultaneously using the CCD's spatial resolution. For each ion we select a box or region of interest (ROI) that determines the pixels over which the CCD will integrate to determine the ion's state. Ion ROI box edges are positioned on adjacent pixels with no overlap to maximize detection fidelity and on-chip binning is used to enhance readout speed.

Figure 2.7a and b shows detection histograms and the actual CCD "pictures" for three ions prepared in the $|\mathbf{000}\rangle$ dark state and the $|\mathbf{111}\rangle$ bright state. In fig. 2.7c we show the detection histograms and post-selected examples of all possible pictures for an equal superposition state achieved by preparing the state $|\mathbf{000}\rangle$ and then applying a microwave $\pi/2$-pulse at the hyperfine splitting $\omega_{\mathrm{HFS}}/2\pi = 14.530$ GHz equally on

the three ions to produce the state $(|\mathbf{0}\rangle + |\mathbf{1}\rangle)^{\otimes 3}$.

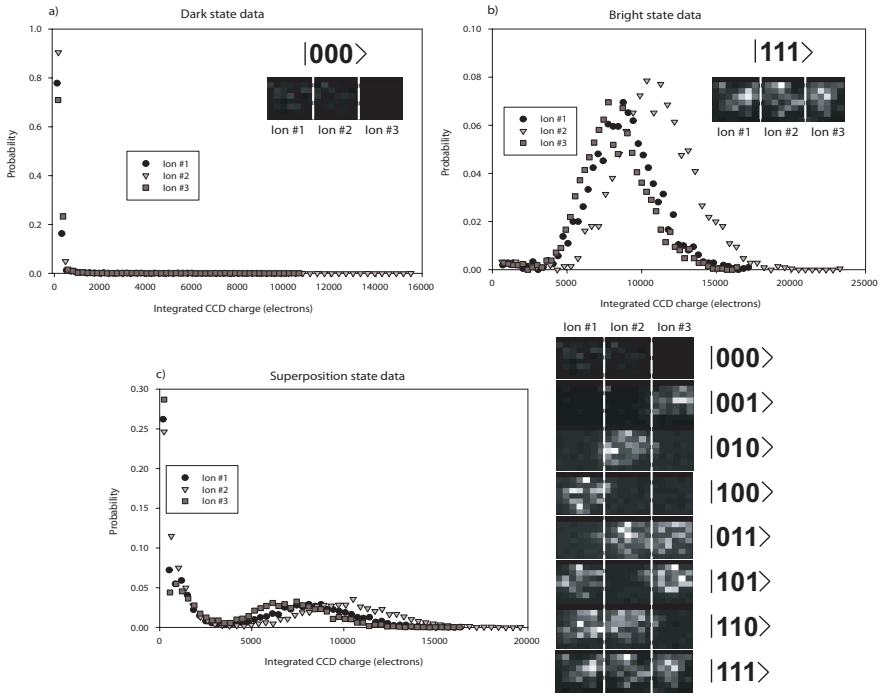

Figure 2.7: Detection histograms for three ion qubits using a CCD. The qubits are in the states: a) $|0,0\rangle \equiv |\mathbf{0}\rangle$; b) $|1,0\rangle \equiv |\mathbf{1}\rangle$; and c) an equal superposition state prepared by starting in $|\mathbf{000}\rangle$ and applying a microwave $\pi/2$-pulse equally on all three qubits to produce the state $(|\mathbf{0}\rangle + |\mathbf{1}\rangle)^{\otimes 3}$. Each graph contains 4000 trials. Note that middle ion #2 has the most integrated counts due to unequal illumination by the detection beam. Adjacent to each histogram are examples of the post-selected single-shot images acquired by the CCD for each case: a) all "dark" ($|\mathbf{000}\rangle$); b) all "bright" ($|\mathbf{111}\rangle$); and c) all combinations of "dark" and "bright". The dashed white lines indicate the boundaries of the regions of interest used to determine the qubit state via integrated CCD counts.

2.6.2 Possible additional errors In addition to the single-ion detection errors due to off-resonant coupling (sec. 2.2), simultaneous multiple ion detection on a CCD can produce some additional errors. One possible error is that the detection beam has a waist of ~ 10 μm, compared to an ion-ion spacing of ~ 4 μm for this experiment, leading to unequal illumination of the ions (visible in the histograms of fig. 2.7 where the middle ion (#2) is brighter than the outer two ions). In general, this unequal illumination results in different constant offsets for each ion's light level that are easy to correct.

The more significant error source is the potential for adjacent ion effects (particularly optical pumping from adjacent ions) or box-to-box overlap on the CCD. Pumping an ion into the "bright" state from the fluorescence of the adjacent state is completely neglible compared to the effect of the laser. The light intensity due an adjacent bright ion is: $\frac{\hbar\omega\gamma/2}{4\pi x^2}$ where ω is the frequency of the radiated light and x is the inter-ion spacing. In comparison, the laser intensity is typically: $I_{\text{laser}} \approx I_{\text{sat}} = \frac{\pi\hbar c\gamma}{3\lambda^3}$ where λ is the wavelength of the radiated light. Thus, the light intensity effect of the adjacent ion relative to the laser is:

$$\frac{I_{\text{ion}}}{I_{\text{laser}}} = \frac{3\lambda^2}{4\pi x^2}. \tag{2.24}$$

For $^{111}\text{Cd}^+$, $\lambda = 214.5$ nm and with three ions in a trap with $\omega_z/2\pi \approx 850$ kHz, $x \approx 4\ \mu$m. Thus, the ratio of illumination intensities due to the adjacent ion and the laser is: $I_{\text{ion}}/I_{\text{laser}} \approx 7 \times 10^{-4}$.

Overlap or spreading of one ion's light into the ROI of adjacent ions can be most clearly seen by examining the conditional probabilities of the ions dependent on the state of the other ions. By independently rotating the qubits with microwave pulses, there should be no correlation between qubit states, but light overlap between boxes would produce such correlations. Using the data of figure 2.7 we find that adjacent ion pairs (left/center and center/right) exhibit conditional probability correlations of $\sim 1.2\%$. With this overlap, the detection fidelity for individual qubits in the presence of other qubits is $\sim 98\%$. This fidelity is fully consistent with a small amount of spreading of the light from one ion into the ROI of the adjacent ion, an effect most likely caused by ion/imaging system drifts over a few minutes. Further mechanical stabilization of the imaging system should eliminate this drift.

In summary, we have developed a general theory for ionic qubit state detection and applied that theory to the specific examples of $^{111}\text{Cd}^+$ and $^{171}\text{Yb}^+$. We have also

experimentally demonstrated simultaneous multi-ion detection using an intensified CCD. Future improvements are discussed in sec. 5.2.1.

CHAPTER III

Multi-Zone "T" Ion Trap

3.1 Introduction

In chapter II we discussed and demonstrated qubit state detection of multiple qubits stored in a single trapping region. Extending this measurement ability to large numbers of qubits requires not only a high-fidelity entangling gate [47], but also the ability to trap and manipulate the physical arrangement of multiple atomic ions. In this chapter we explore a multi-zone "T" trap consisting of an array of ion traps so that individual ions can be reliably shuttled between physical locations.

Shuttling of trapped ions along a line between adjacent trapping zones and separation of two or more ions has been previously demonstrated [23, 24, 25, 20, 22]. Note, however, that current entanglement techniques are most effective (produce the highest fidelity) when acting on only two ions in a particular ion trap. Using this pair-wise entanglement build-up requires the ability to physically co-locate *any* two ions in a trapping region to perform the entangling operation. Thus, "linear" separation and shuttling is not enough to bring together arbitrary pairs of ions. In this chapter, we discuss the necessary general requirement of shuttling ions in two dimensions.

3.2 Trap Construction and Usage

The main ion trap geometry used for multi-qubit quantum information processing is the linear rf-quadrupole trap, where ions are transversely confined to the nodal axis of an rf quadrupole potential supplied from nearby linear electrodes. Axial confinement is then accomplished by segmenting the linear electrodes and applying differential static potentials along the axis. This technique allows for quasi-independent control of the ions in the transverse and axial directions.

In order to fabricate complex ion trap arrays, the electrodes can be constructed from multi-layer planar substrates. To design a trapping geometry capable of supporting a two-dimensional junction, the electric field topology near the junction must be considered carefully. While two-layer substrate geometries provide strong confinement in both transverse dimensions inside a linear chain of trapping regions, it is difficult to have sufficient transverse confinement in the junction region where the intrisic two-dimensionality of the trap must manifest itself [48, 49]. Instead, we use a symmetric three-layer substrate geometry (fig. 3.1) that allows confinement throughout the junction region. The middle-layer carries the rf potential and segmented outer-layers (each identical) carry control voltages that are used to confine the ion along the axial dimensions of the trap sections.

The trap electrodes consist of gold-patterned alumina substrates which are laser-machined and polished to a thickness of 125 μm for the middle (rf) layer and 250 μm for the outer (control) layers. The laser-machining produces substrates with a T-shaped channel that will provide the "track" along which the ions will move. Gold is deposited on the rf electrode using an electron beam evaporator while the necessary segmenting of the outer control electrodes requires using dry-film photolithography

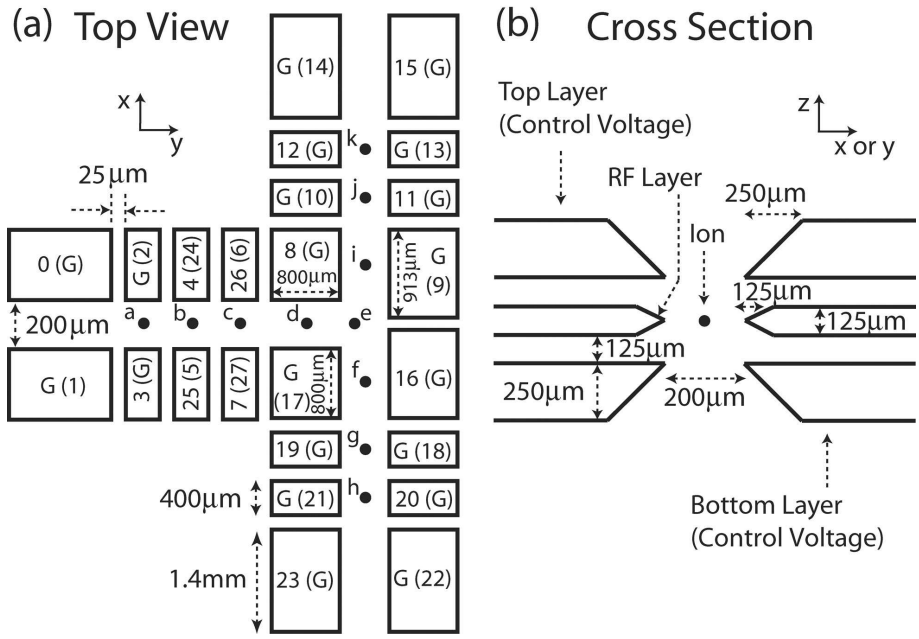

Figure 3.1: Top view and cross-section of two-dimensional "T" trap array. Dots depict the location of trapping zones, labelled a-k. The outer control electrodes are labelled 0-27, with bottom layer electrodes in parentheses. Electrodes labeled by G are internally grounded.

and wet-chemical etching to deposit 400 nm of gold on top of a 15 nm titanium layer.

The substrates are assembled by hand using spacer rings to separate the electrodes by 125 μm and alumina mount bars at the edges to hold the three layers together. The control electrodes need to be isolated from external noise and from induced rf caused by the nearby rf electrodes. This shielding is accomplished via a "pi-filter network" where each electrode is connected to a $C = 1$ nF capacitor shunted to ground and then connected in series to a $R = 1$ kΩ resistor leading to the vacuum feedthrough ($\omega_{3dB}/2\pi = 1$ MHz). These chip capacitors and resistors are ribbon-bonded onto a gold coated quartz plate that is mounted adjacent to the alumina substrates. The quartz plate proved very successful at holding the circuit elements, but extreme care must be taken when drilling and handling the quartz plate and particularly when strain-relieving the wires leading to the vacuum feedthrough.

During usage, ions can be confined in any of the 11 trapping zones labeled by let-

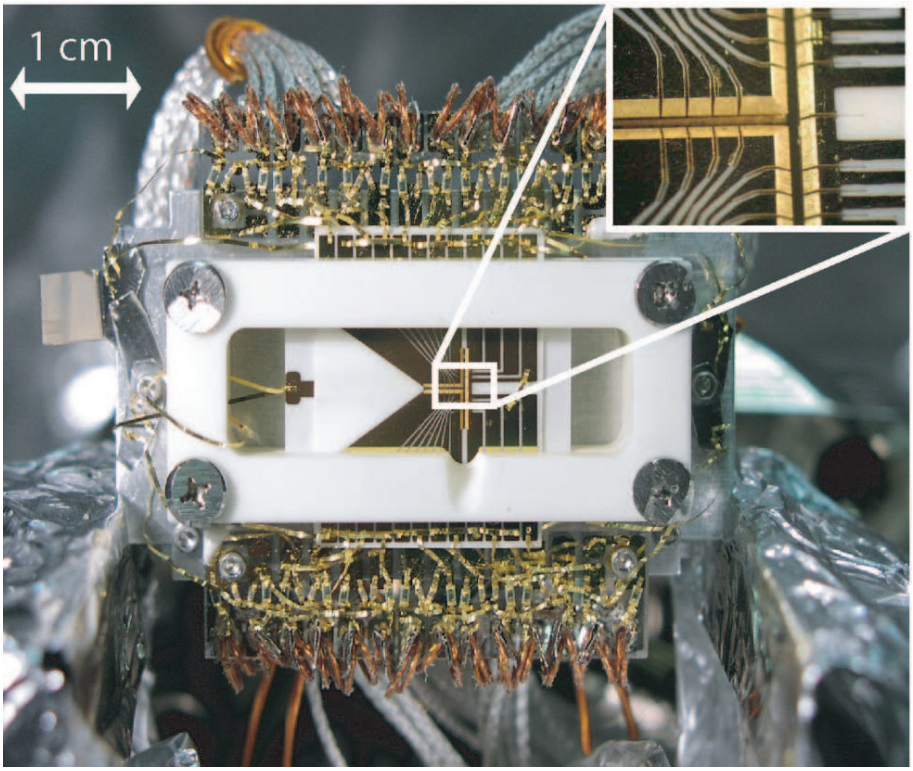

Figure 3.2: Photograph of T-junction trap array. The magnified inset shows the trapping array near the junction.

ters a-k in figure 3.1. Due to the trap's relatively large size and symmetric geometry, successful trapping parameters are reasonably flexible. For the results discussed below, we applied rf voltage to the central layer electrode at frequency $\Omega/2\pi = 48$ MHz and amplitude $V_0 \approx 360$ V (successful range: 100 V-500 V). This results in a transverse ponderomotive secular frequency of $\omega_{rf}/2\pi = 5.0$ MHz for the trapping zones a, b, c, j, k, g, and h.

Voltages applied to the 28 control electrodes to produce axial confinement are computer-controlled using NI 114 PCI cards hooked up to NI BNC-2110 interface boxes. The coaxial BNC output from these interface boxes (maximum range: -10 V to +10 V) is then directed to a home-built amplifier system consisting of Apex PA85A amplifier chips powered by Acopian B125GT40 power supplies. The resulting BNC output is wired to a vacuum interface box where a pi-filter network ($C = 1$ nF,

$R = 1$ kΩ, and $\omega_{3dB}/2\pi \approx 1$ MHz) reduces noise. Wires are then directly attached to a 35-pin vacuum feedthrough before continuing to the quartz filter plate arrangement. Note that control voltages of ~ 100 V result in axial secular frequencies of ~ 2.5 MHz for traps whose central segment is 400 μm wide.

The ion is imaged with a CCD camera to a nearly diffraction-limited spot with f/2.1 optics. The imaging system was optimized to view an area of approximately 550×550 μm which allows for the simultaneous observation of trapping zones d and i, or d and f (fig. 3.1), permitting real-time observation of a corner-turning shuttling protocol. At this magnification, a diffraction-limited image of the ion encompasses a few pixels which is visible above the background fluctuations of the image.

3.3 Ion Shuttling Control

With the ability to observe the ion's movement between trapping regions, we have implemented various key composite trapped-ion shuttling protocols: linear shuttling, corner turning, and separation/combination of two ions. Using these building blocks, high level shuttling procedures can be implemented.

3.3.1 Linear shuttling As a straightforward example that illustrates the rationale behind shuttling protocol design, consider linear shuttling between trapping regions a and b. As illustrated in figure 3.3, we start with the ion in zone a by placing positive voltage on electrodes 0, 1, 4, and 5 while applying negative voltage on electrodes 2 and 3. Qualitatively we then need to set a "wall" for the ion by applying positive voltage to electrodes 6 and 7. We then "elongate" the trap by lowering the voltage on electrodes 4 and 5 to produce a trap with an effective width of ~ 800 μm (regions a and b combined). During this time the axial trap frequency will necessarily be at its lowest since the control electrodes are twice as far away. We then bring up the

voltage on electrodes 2 and 3 to reconstitute a tighter trap in zone b.

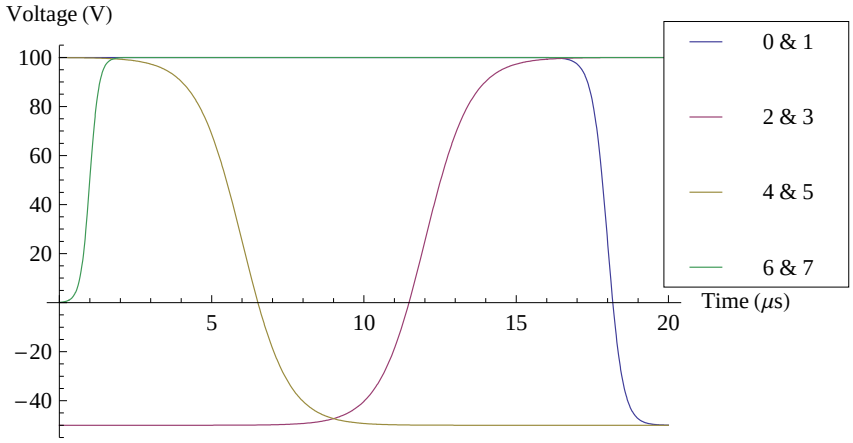

Figure 3.3: Voltage pattern for linear shuttling between regions a and b in T-trap.

Finding a protocol that optimizes the speed of this process while minimizing the heating of the ion is an involved problem that is discussed extensively in [50]. Here, we simply note that a smooth voltage change on a time scale slower than the ion's periodic motion in the trap results in adiabatic shuttling that does not appreciably heat the ion. Precise timing of the voltage can allow for low heating even with changes faster than the ion's motion in the trap, but the level of control necessary makes this type of protocol technically challenging.

3.3.2 Corner turning The shuttling of ions through the T-junction merits special attention. Due to the geometry of the junction, there is complete transverse confinement throughout the T-junction. However, there are linear rf nodes leading towards the junction from all three directions that give way to small humps in the ponderomotive potential as the junction is approached, leading to a point node in the rf potential near the center of the T-junction (trapping zone e). These rf humps are small compared to the overall transverse ponderomotive potential walls, so time-varying voltages on the control electrodes can be used to push the ion over the rf

humps.

Thus, shuttling a single atom around a corner requires a tradeoff: the time-varying pushing potentials must be strong enough to overcome the rf humps, but not so strong as to de-stabilize the trap in the transverse directions. Moreover, stronger pushing potentials will result in faster ion transport but also in more ion heating. Therefore, the control voltage sequence must be carefully synchronized with the motion of the ion. Fast, non-adiabatic voltage changes inside the trapping region may be required to minimize the kinetic energy acquired by the ion and to overcome the second hump upon emerging from the junction.

Figure 3.4 shows voltages applied to the electrodes carrying control voltages in order to shuttle the ion around the corner from trapping zone d to i. The success rate of the corner-turning protocol was measured to be 99.9% (881 out of 882 attempts). Simulations predict that the ion acquires about 1.0 eV of kinetic energy during the corner-turning protocol. This energy is dissipated via Doppler cooling, but sympathetic cooling can also remove this energy in order to preserve the internal state of the ion. It should be noted that, in principle, the gain in kinetic energy can be reversed with fast phase-sensitive switching of the trapping potentials without using any dissipative force.

In order to shuttle the ion back from the top of the T into the stem, a voltage sequence is used that corresponds approximately to the above corner-turning protocol but spatially reflected about the axis connecting electrodes 8 and 16. The success rate for this protocol was measured to be in excess of 98% (118 attempts). This sequence is conducted at slower speeds (20ms for the whole sequence) but refining the control voltage protocol may allow shuttling times on the order of microseconds.

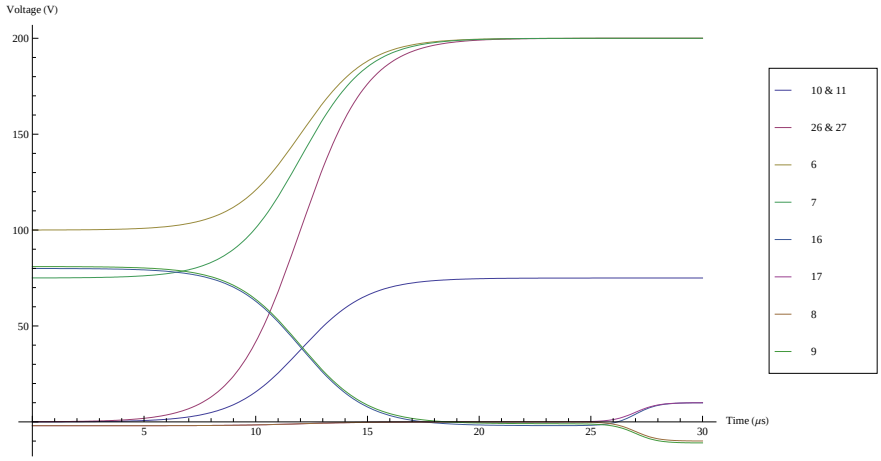

Figure 3.4: Voltage pattern for corner shuttling between zones d and i in T-trap.

3.3.3 Separation/combination A separation protocol is implemented inside the stem of the T array starting from zone b. Trapping zone b is weakened to $\Omega_y/2\pi \approx 20$ kHz to allow for more physical separation of the ions (due to their Coulomb repulsion). Then a potential wedge separating the two ions is slowly brought up using electrodes 4 and 5, with electrodes 0, 1, 8 and 17 being used to confine the ions along the y-axis. Separation typically takes ~ 10 ms and is carried out with a success rate of only $\sim 58\%$ (64 attempts), possibly limited by the very weak trap during separation and the large (400 μm) axial extent of the control electrodes.

Using these key protocols a composite protocol was successfully implemented for switching the position of two ions. The ions are separated in zone b, the first ion transferred to j, the second to h. The first ion is shuttled back to b. The second ion is shuttled back to b, having switched places with the first ion, with the two-ion chain effectively executing a three-point turn. The protocol was carried out in multiple successive 10 ms steps. Conditional on successful separation and recombination, we obtain a success rate of 82% (34 attempts). The success rate for the whole process including separation and recombination is 24% (51 attempts), mainly limited by

separation and recombination efficiency.

CHAPTER IV

Cadmium Magneto-Optical Trap: Computer Simulations and Experimental Results

4.1 Introduction

The magneto-optical trap (MOT), first realized in 1986 [51, 52], forms the basis of much of modern experimental atomic physics. The MOT technique can act as the first step towards BEC/BCS production [53, 54] or optical lattice experiments [55], or it can be used to confine atoms for direct studies of precision atomic spectroscopy [56], cold collisions [57], atom interferometry [58], or the generation of quantum-degenerate gases [59], to name a few examples. Typically, nearly all cold atom experiments have dealt with the alkali atoms, but there has been some progress in the trapping of two-electron atomic species such as Ca [60], Mg [61], Sr [62], and Yb [63].

Our focus in this chapter will be the trapping of neutral Cd atoms, which have two valence electrons, in a deep-ultraviolet MOT operating on the $^1S_0$ to $^1P_1$ transition at $\lambda = 229$ nm. After first describing the necessary experimental apparatus for confining Cd atoms in a MOT, we examine a computer-based simulation of atomic behavior in the MOT with a particular eye towards modeling trap loss mechanisms which can then be compared with experimental data.

4.2 Experimental Realization of Cadmium MOT

Confining neutral Cd atoms in a MOT requires some unique experimental considerations compared to previous MOT experiments. Cadmium has eight stable isotopes, six of which are relatively abundant, but note that due to the large isotope shift only one isotope can be trapped at a time using a monochromatic incident laser beam. Figure 4.1 shows the electronic structure of Cd for both bosons (nuclear spin I=0, even isotopes) and fermions (I=1/2, odd isotopes). Note that the hyperfine splitting present in the $^1P_1$ states of the fermionic isotopes prevents using standard MOT techniques to trap ^{111}Cd and ^{113}Cd (see sec. 5.2.3).

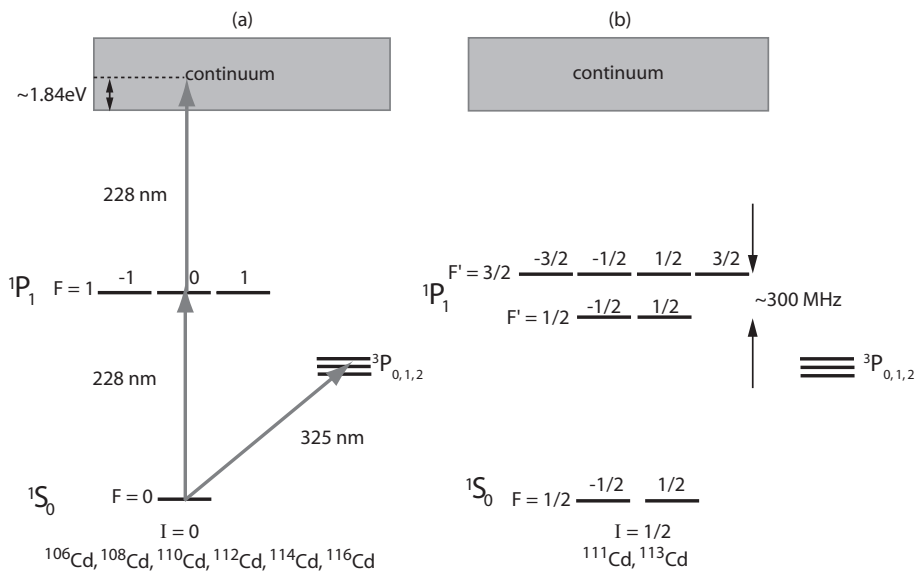

Figure 4.1: Neutral Cd energy level diagram. a) The bosonic (even) isotopes (I=0) of Cd. b) The fermionic (odd) isotopes (I=1/2) of Cd, where the $^1P_1$ hyperfine splitting arises from (L · I) coupling. Individual levels are labeled with m_F. Note that diagram is not to scale.

In our experiments with bosonic Cd (I=0, even isotopes), the $^1S_0$ to $^1P_1$ atomic transition used for the MOT occurs at a wavelength of $\lambda = 228.8$ nm with an excited state lifetime of $\tau = 1.8$ ns (radiative linewidth $\gamma/2\pi = 91$ MHz) and saturation intensity of $I_{sat} = \pi hc\gamma/(3\lambda^3) \approx 1.0$ W/cm^2. For comparison, the saturated photon

recoil acceleration on a Cd atom is $a_0 = h\gamma/2m\lambda = 4.4 \times 10^5 g$, which is 50 times that of Rb (here g is the acceleration due to gravity and m is the mass of a single Cd atom). We confine Cd atoms in a vapor-cell so background gas collisions lead to loss of trapped Cd atoms. However, since the 228.8 nm trapping light can also excite atoms from the $^1P_1$ state directly to the ionization continuum this introduces an additional photoionization loss on the trapping process. We can investigate this loss process to experimentally determine the photoionization cross-section of the $^1P_1$ state (sec. 4.3). Moreover, photoionization loss provides an opportunity to reliably create cold ions and atoms at the same location [64] for the investigation of ultracold atom-ion interactions [65, 66] (see sec. 5.2.4).

A schematic of the experimental apparatus is shown in figure 4.2. Due to Cadmium's large linewidth, high magnetic field gradients are required to shift the Zeeman levels sufficiently for the atoms to feel a substantial trapping force at the edge of the laser beams (a rough guide is that the optimum Zeeman shift is one linewidth at the beam waist). Experimentally, we use NdFeB permanent ring magnets with a 2.54 cm outer diameter, 0.64 cm inner diameter, and 0.95 cm thickness that are mounted coaxially on xyz translational stages. By adjusting the axial separation of the magnets we can achieve magnetic field gradients of $\sim 150 - 1500$ G/cm at the trap center, which produces the desired Zeeman shift for our beam sizes.

The trapping beams are generated with a frequency quadrupled Ti:Sapphire laser, yielding 2.5 mW at 228.8 nm (see appendix A). The ultraviolet light is split into six independent trapping beams in order to better control the intensity balance of the counter-propagating beams. We observe that the MOT can withstand an intensity imbalance of 10% between a pair of beams (see appendix B), and we can balance the intensity between any pair of counter-propagating beams to better than 5%.

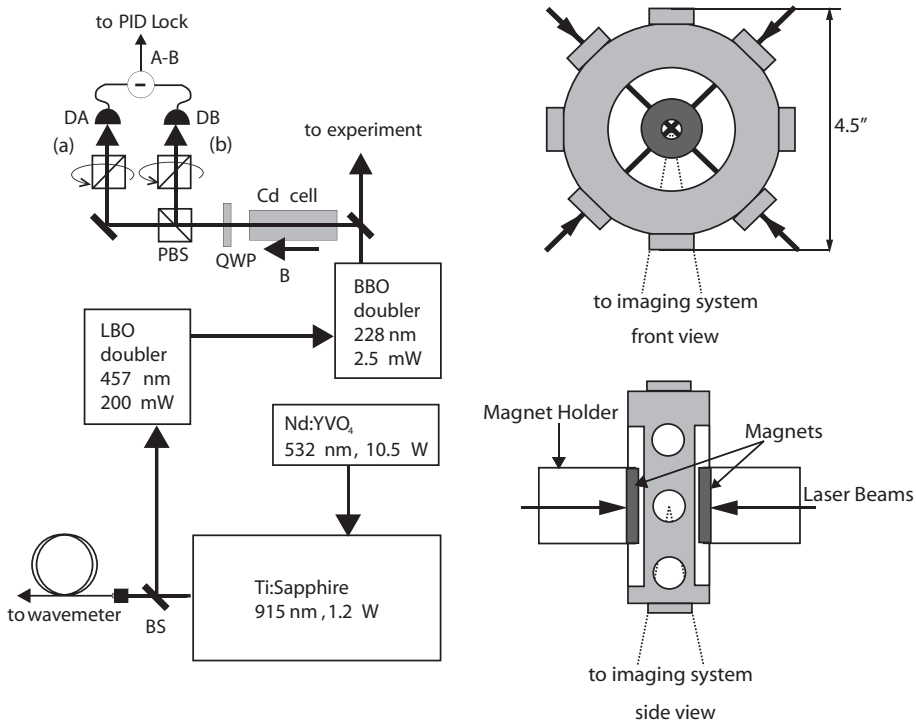

Figure 4.2: Schematic diagram of MOT laser system and vacuum chamber. Left: Schematic diagram of the laser system and the laser lock (DAVLL). The laser lock consists of the Cd cell, a quarter wave plate (QWP), a polarizing beam splitter (PBS), and two photodetectors (DA, DB) for path a and b, respectively. Right: The MOT vacuum chamber and the laser beam geometry. The MOT is formed by 6 independent beams. The imaging system sits below the chamber, and the dark shaded regions are the NdFeB magnets.

Typical beam waists range from $w_0 = 0.5 - 1.5$ mm and the total power ranges from $P = 0.7 - 2.0$ mW, resulting in peak intensities ranging from $I = 0.03 - 0.5$ W/cm^2.

Approximately 200 μW is split from the main laser beam and directed to a small cadmium vapor cell to stabilize the laser frequency. We use a dichroic atomic vapor laser lock (DAVLL) [67, 68] operating on the $^1S_0$ to $^1P_1$ transition in Cd. Using DAVLL stabilization as opposed to saturated absorption locking techniques has the advantage of reducing the necessary power while allowing small frequency adjustment. In practice, the cell is heated to 80° C to increase optical absorption to $\sim 80\%$ through the 5 cm cell. A uniform magnetic field, produced by NdFeB permanent ring magnets placed cylindrically around the cell, is applied along the laser beam axis to lift the degeneracy of the $^1P_1$ states. When linearly polarized light is sent through the cell the difference between absorption of the Zeeman-shifted σ^+ and σ^- transitions produces a dispersive-shaped signal. We can extract this signal by using a polarizing beam splitter to be able to independently measure the σ^+- and σ^--polarized beams. With the detectors wired oppositely, directly combining the two electrical signals allows us to lock the laser to the zero crossing point. The capture range is determined by the Zeeman splitting between the two transitions, or about 1.5 GHz in a 500 G field. To change exact laser frequency we move the zero crossing point by attenuating the laser power in one of the polarization paths (a or b) after the cell (see figure 4.2). This method proves far more stable than using an electronic offset method where we would be senstive to small voltage drifts. The lock is stable to within 30 MHz, or 0.3γ, over the 1.5 GHz capture range, and the dominant sources of fluctuations are beam-steering drifts and birefringence fluctuations of the cell windows from temperature changes over times greater than 1 second.

4.2.1 Cd MOT Vapor Cell We produce and confine Cd atoms in a vapor cell where the radiative forces accumulate atoms following the rate equation:

$$\frac{dN}{dt} = L - \Gamma N - \beta \frac{N^2}{V}, \tag{4.1}$$

where N is the number of trapped atoms, L is the loading rate, Γ is the loss rate related to single atom effects, β is the loss rate due to binary collisions within the trap, and V is the effective volume occupied by the trapped atoms [69, 70, 71, 72]. Using simple kinetic gas theory at constant temperature one can show that $L \approx nV_c^{2/3} v_c^4 / v_{th}^3$, where V_c is the capture volume, v_c is the capture velocity [69], v_{th} is the thermal velocity, and n is the density of Cd atoms in the background vapor [73, 74].

When the MOT density is low ($< 10^9$ cm^{-3}), the atoms are essentially non-interacting and we expect the density to be limited by the cloud temperature. In this regime the spatial distribution of trapped atoms is expected to be Gaussian with a cloud radius that is independent of the trapped atom number. This contrasts with high density ($> 10^{10}$ cm^{-3}) MOTs where effects such as reradiation must be considered [75]. The Cd MOT reported here operates in the low density regime, so the last term of eqn. 4.1 can be neglected since it describes collisions between two trapped atoms. But unlike conventional alkali MOTs, where single atom loss mechanisms primarily involve collisions between trapped atoms and the background gas, Cd (like Mg) has an additional single atom loss term due to photoionization [76, 77].

Thus, with these conditions, solving eqn. 4.1 for the steady state number of trapped atoms yields: $N_{ss} = L/\Gamma$. The total loss rate, Γ, is given by the sum of loss rates due to background collisions and photoionization:

$$\Gamma = \Gamma_0 + \Gamma_{\text{ion}}, \tag{4.2}$$

where Γ_0 represents the rate at which trapped atoms are ejected due to collisions with the background vapor (dominated by Cd) and Γ_{ion} is the photoionization rate. The photoionization rate can be written as:

$$\Gamma_{\text{ion}} = \frac{\sigma_{PI} P(I,\delta) I}{\hbar\omega}. \tag{4.3}$$

Here, σ_{PI} is the photoionization cross section, $\hbar\omega$ is the photon energy, I is the total MOT laser beam intensity, and $P(I,\delta)$ is the fraction of trapped atoms in the excited state ($^1P_1$) defined as:

$$P(I,\delta) = \frac{1}{2}\frac{s}{1+s+4\delta^2}, \tag{4.4}$$

where $\delta = \Delta/\gamma$ is the laser detuning scaled to the natural linewidth and $s = I/I_{\text{sat}}$ is the saturation parameter.

The MOT chamber contains a 1 cm long hollow stainless steel tube of diameter 0.1 cm packed with about 0.02 g of pure Cd wire. We can control the background Cd vapor pressure throughout the entire chamber by heating this small oven. When we direct the trapping beams into the chamber we see tracks of fluorescing Cd within the extent of the laser beams. Based on this atomic fluorescence, we estimate the background Cd vapor pressure to range between approximately 10^{-11} torr with the oven off to about 10^{-10} torr with the oven at approximately 300° C. We speculate that the Cd atoms sublimated from the oven do not readily stick to the chamber surface, resulting in good control of the Cd vapor pressure with the small oven. We note that the vapor pressure of Cd is predicted to be 10^{-11} torr at room temperature [78], which is consistent with our observations.

4.2.2 Detecting Neutral Cd Atoms in a MOT The atomic fluorescence from the trapped atoms is collected with an f/3 lens (solid angle of $d\Omega/4\pi = 0.6\%$) and imaged onto an intensified charge coupled device (ICCD) camera. Every photon incident on

the camera yields $\eta G \simeq 65$ counts, where $\eta = 20\%$ is the quantum efficiency of the camera and G is the ICCD gain factor. Including an optical transmission of $T \approx 50\%$ in the imaging system, we expect a total count rate of $\gamma P(I, \delta) G \eta T (d\Omega/4\pi) \approx 10^7$ counts/sec from each trapped atom in the MOT. In this way, we relate the total fluorescence count rate to the number of atoms in the MOT, with an estimated accuracy of 50%. For various settings of the MOT parameters, we are able to observe between $\sim 10 - 3000$ atoms in the MOT.

Note that CCD count fluctuations in this imaging setup can arise from laser intensity / detuning changes or from CCD intensifier fluctuations (since electron avalance production is a stochastic process). When attempting to view small numbers of atoms and determine the exact number of atoms, these fluctuations have noticeably different effects. In essence, gain fluctuations act as a multiplicative error that affects both background and atomic signal whereas laser fluctuations only affect the atomic signal since the background is insensitive to laser parameters. Figures 4.3 and 4.4 show simulated histograms for various values of intensity and gain fluctuations, respectively. Note that experimentally we operate in the regime where intensity fluctuations are the dominant factor.

4.2.3 First-time MOT Production/Observation With a MOT already in place, optimizing its characteristics is typically a relatively easy process. But producing a small-beam MOT for the first time can be quite challenging, so here we discuss some strategies for initial alignment.

We have found that with the small beams necessitated by the technical difficulties of producing UV laser radiation, the importance of laser beam self-overlap and beam overlap with the magnetic field null cannot be overstated. We have found that making the entire vacuum chamber moveable greatly facilitates this alignment. First, align

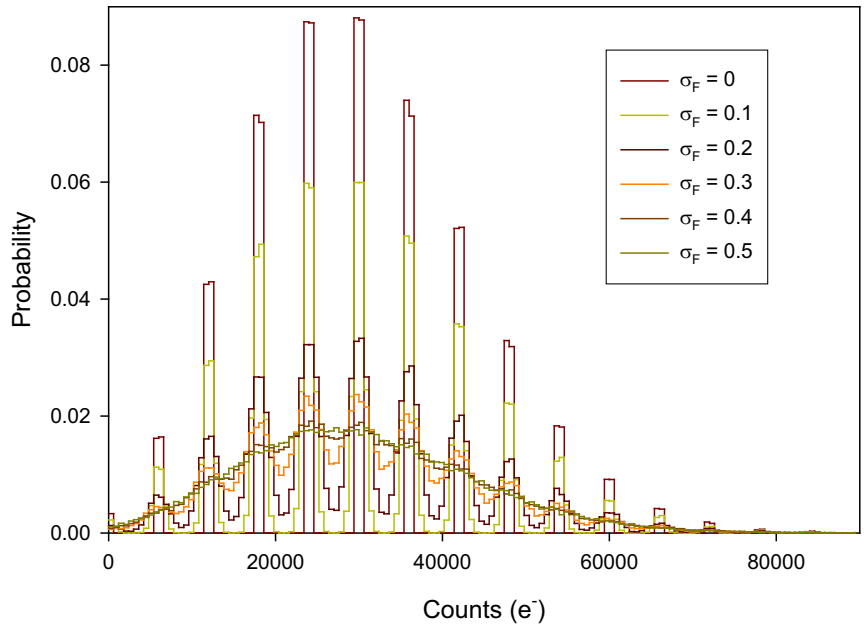

Figure 4.3: Histogram of integrated CCD counts for MOT atom detection with varying intensity fluctuations.

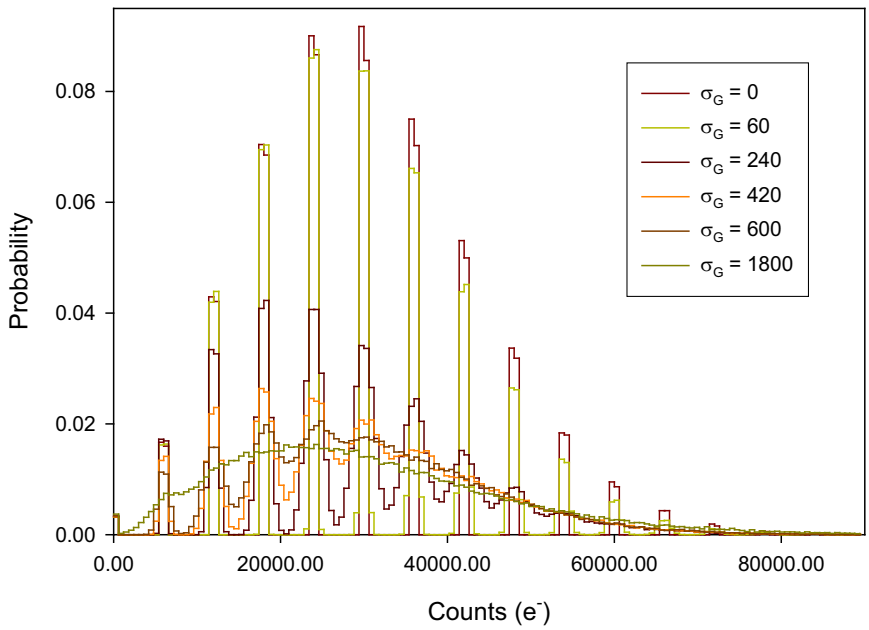

Figure 4.4: Histogram of integrated CCD counts for MOT atom detection with varying gain fluctuations.

the imaging system so that its field of view is centered on the area of probable future MOT production. Then remove the vacuum system and align the six beams in free space so that they overlap. Next, use the Gauss probe to place the magnetic field zero on top of the beam crossing. This may suffice for an initial search or one can further refine the beam alignment by determining if insertion of the vacuum chamber produces any beam shifts and correcting for them in advance.

When it is time to actively search there are many parameters that need to be adjusted. We have found that in the absence of a definite knowledge of the laser trapping frequency, it is most efficient for two people to conduct the search. One person manually controls the laser frequency while carefully watching and adjusting the computer search program. The other person adjusts the magnetic field alignment and spacing while also changing the laser beam alignment. Personal preference seems to dictate the success of any particular alignment method, but all successful methods rely on a methodical search of the parameter space that eliminates the need for backtracking.

Initially the ill-formed MOT may resemble a slightly brighter halo in one area of the CCD's visual field and it may form and dissipate rapidly resulting in bright flashes (most likely due to the laser being near resonance and drifting to the blue of the cooling transition). The most direct way of testing whether an apparant build up of atoms is truly a MOT is to block only one of the six cooling beams or to change the magnetic field. Either change should result in an immediate disappearance if the candidate is indeed a MOT. Note, unfortunately, that blocking a beam or moving the magnets can change the scatter and can lead to deceiving tests.

The most conclusive test is to slowly ($\sim$ 1 GHz/minute), controllably scan the laser cooling frequency. If a MOT is present, dramatic increases in atomic fluoresence

will be visible at frequencies that correspond to the resonance of each atomic isotope (figure 4.5). Note that not all isotopes are easily trapped or visualized, so scanning the laser frequency is a particularly important procedure when searching for a MOT.

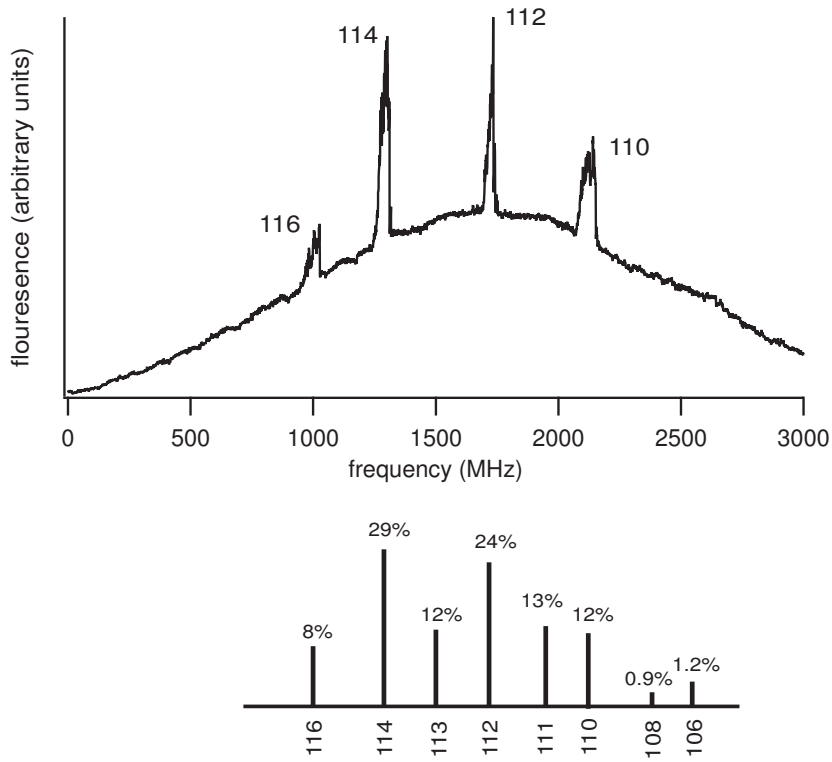

Figure 4.5: Scan of MOT trapping radiation frequency. Top: Scan across frequency showing the different Cd isotope MOTs. The underlying curve is the Doppler fluorescence profile of the Cd atoms. At certain frequencies there is a large build up, due to the MOT accumulation as its resonance is crossed. Bottom: Natural abundance of neutral cadmium isotopes. Out of these eight isotopes, we are only able to clearly observe trapping of the four most abundant bosonic (even) isotopes.

4.3 Experimental Determination of Cd Cross-Sections

In figure 4.6, the filling of the MOT is shown for Cd vapor pressures of approximately 10^{-10} torr and 10^{-11} torr. Note that the filling time for the MOT is determined by the loss rate of atoms from the MOT (eqn. 4.1). Unlike conventional vapor cell MOTs, we find that the filling time (loss rate) is independent of the background pressure, while the steady-state number of atoms in the MOT is strongly dependent

on pressure. This indicates that collisions with the background gas have very little effect on the loss rate and instead we are limited by photoionization loss from the MOT beams. This is investigated in more detail by measuring the filling time (loss rate) as the MOT laser intensity is varied, as shown in figure 4.7. We observe a roughly quadratic dependence of loss rate on intensity, consistent with eqn. 4.3. The extrapolated loss rate at zero intensity is much smaller than all of the observations, directly indicating that $\Gamma_0 \ll \Gamma_{ion}$, or that the loss rate in this experiment is dominated by photoionization.

From this measurement we can also directly extract the photoionization cross section from the $^1P_1$ state, given measurements of the intensity, excited state fraction P(I,δ), and the known wavelength of the light. We find that the photoionization cross section of the $^1P_1$ state of Cd from the 228.8 nm light is $\sigma = 2(1) \times 10^{-16}$ cm^2, with the error dominated by uncertainties in the laser intensity and detuning. This result is within an order of magnitude for the measured cross sections of other two electron atoms [76, 79].

4.4 MOT Computer Simulation

In this section we describe the development of a 3-dimensional, Monte Carlo computer simulation to calculate the loading rate for our Cd MOT. Some analytical models have been developed to determine the loading rate from an atomic beam [47], but the simplifying assumptions necessary to produce an analytical solution (particularly neglecting the effect of the magnetic field) make these methods less reliable for predicting typical MOT loading behavior. For Cd in particular, the large B-fields necessary to produce the MOT are likely to make any analytical models too rough to provide any predictive or explanatory power.

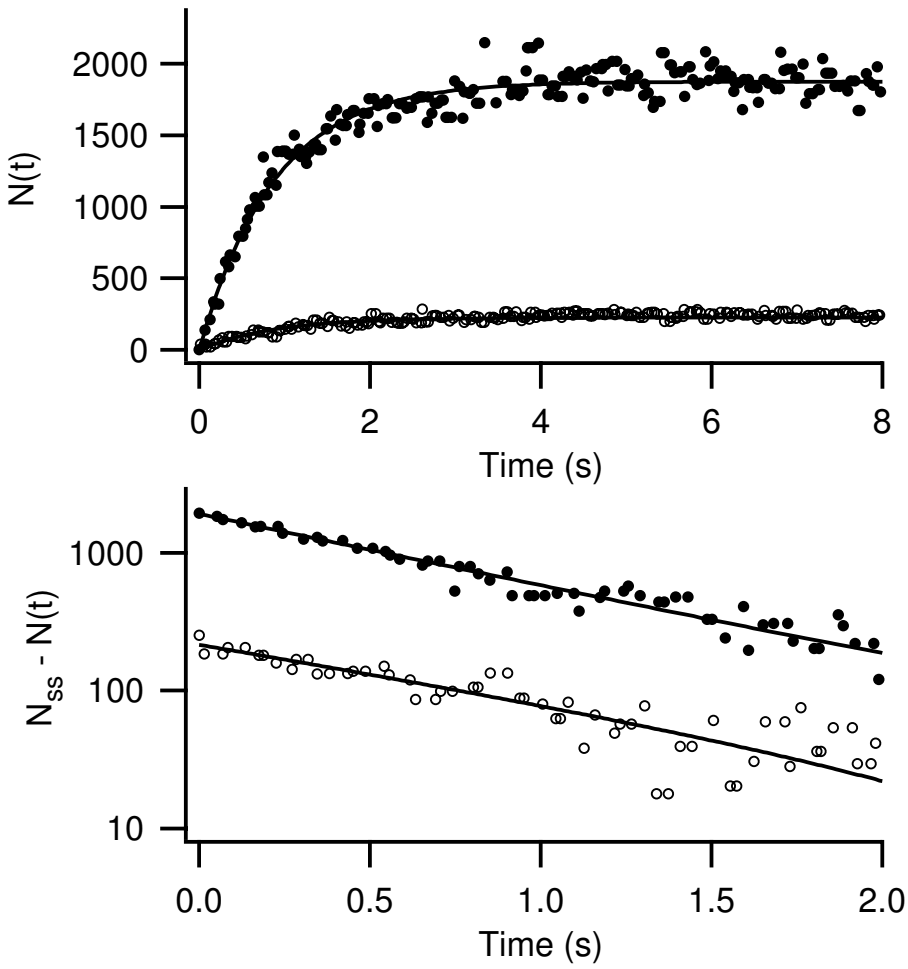

Figure 4.6: Observed trapped atom population behavior for different background pressures. Top: Observed trapped atom number N(t) for two different Cd background vapor pressures. The top curve corresponds to a pressure of 10^{-10} torr and the lower curve corresponds to 10^{-11} torr. By fitting the data to a growing exponential, $N(t) = N_{ss}(1 - e^{-\Gamma t})$, we find that the filling time, Γ^{-1}, is approximately 1 sec for each case. This is clear from the lower logarithmic plot of the data. Bottom: N_{ss}-N(t) plotted for both vapor pressures on a log scale. The filling times are about 1 sec for each curve.

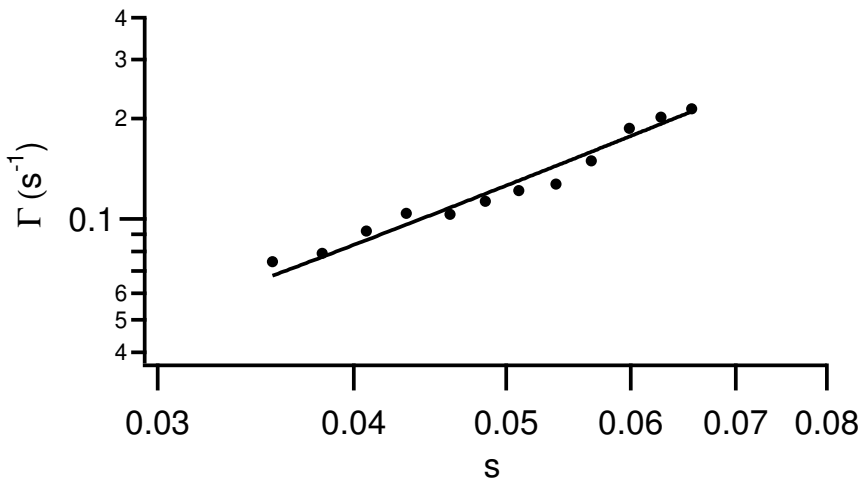

Figure 4.7: Observed MOT loading rate vs. saturation parameter $s = I/I_{sat}$. The power is varied for a constant beam waist of $w = 1.25$ mm. The photoionization cross section out of the $^1P_1$ state is determined from a quadratic fit to s given by eqn. 4.3. Extrapolating the curve to zero intensity (not shown here) gives information on the loss rate due to collisions with background gas.

Here, by including the effects of the magnetic field as well as the laser spatial beam profile, we are able to obtain the steady-state number of atoms trapped in an even-isotope Cd MOT. Previous Monte Carlo simulations of MOT loading rates have used models that calculate the capture velocity for an individual atom and extract the loading rate from v_c [80, 81, 82, 83] or have included individual photon recoil events [84].

In contrast, in this work we treat the atoms as non-interacting, point particles and examine the dynamics of an ensemble of individual atoms under the application of the laser radiation. The atoms are subjected to a time-averaged force, namely we do not track individual photon absorption and re-emission events and instead we calculate the averaged momentum kicks over hundreds of scattering events. The atoms' motional behavior is found by numerically integrating the position- and velocity-dependent radiation force.

Specifically, taking the $\hat{x}$-direction as an example, the net acceleration of an in-

dividual atom is given by the sum of the accelerations due to the $+\hat{x}$ and $-\hat{x}$ laser beams:

$$\begin{aligned} a_x(\vec{r}, v_x) &= \frac{\hbar k \gamma}{2m} s_x(\vec{r}) \Bigg[\sum_q \frac{p_{+,q}(\vec{r})}{1 + s_{\text{tot}}(\vec{r}) + (2\delta_{+,q}(\vec{r}, v_x))^2} \\ &\quad - \sum_q \frac{p_{-,q}(\vec{r})}{1 + s_{\text{tot}}(\vec{r}) + (2\delta_{-,q}(\vec{r}, v_x))^2} \Bigg] \end{aligned} \tag{4.5}$$

where q is the polarization index, and the $\pm$ subscripts correspond to the $+\hat{x}$- and $-\hat{x}$-direction beams, respectively.

The individual beam saturation parameter, s_x, and the total saturation parameter, s_{tot}, are given by:

$$s_x(\vec{r}) = \frac{I_x}{I_{\text{sat}}} e^{\frac{-2(y^2+z^2)}{w_0^2}}, \tag{4.6}$$

$$s_{\text{tot}}(\vec{r}) = 2s_x(\vec{r}) + 2s_y(\vec{r}) + 2s_z(\vec{r}), \tag{4.7}$$

where I_x is the intensity of the $\pm\hat{x}$ laser beams (here assumed to be balanced) and $s_y(\vec{r})$ and $s_z(\vec{r})$ are defined analogously to $s_x(\vec{r})$.

The magnetic field in space determines the local quantization axis for each atom which leads to the fraction of the incoming laser radiation that the atom experiences as $\sigma^{\pm}$- or π-polarized given by:

$$p_{\pm,q}(\vec{r}) = \begin{cases} (\frac{1}{2}[1 \mp \frac{1}{2}\frac{xB'}{B(\vec{r})}])^2, & q = -1 \quad (\sigma^-) \\ (\frac{1}{2}[1 \pm \frac{1}{2}\frac{xB'}{B(\vec{r})}])^2, & q = +1 \quad (\sigma^+) \\ 1 - (p_{\pm,-1} + p_{\pm,+1}), & q = 0 \quad (\pi) \end{cases} \tag{4.8}$$

where $B(\vec{r}) = B'\sqrt{z^2 + \frac{1}{4}(x^2 + y^2)}$ is the magnitude of the magnetic field written in terms of the magnetic field gradient, B', along the strong ($\hat{z}$) axis.

The effective detuning for the atomic transition is given by:

$$\delta_{\pm,q}(\vec{r}, v_x) = (\Delta \mp k v_x)/\gamma + q\frac{\mu_B g_F B(\vec{r})}{\gamma\hbar} \tag{4.9}$$

where $g_F = 1$ is the Landé g-factor. Note that for the even isotopes of Cd, there is no Zeeman shift for π-polarized radiation.

Atoms are initially placed uniformly distributed in position within a simulation volume with a lateral dimension of $6w_0$ (3 beam diameters) and the total number of atoms is chosen to correspond to the background density of the atomic vapor.

For simulating a vapor-cell MOT, the atoms are given initial velocities distributed according to a Maxwell-Boltzmann velocity distribution centered about 0. In our Cd experiment (sec. 4.2), we often use the intra-vacuum Cd oven to increase the background vapor pressure. While the output of the oven is not a true atomic beam, we have experimentally determined that when using the oven the Cd atoms have a net velocity of approximately 16 m/s through the trapping region. We are able to model this "psuedo" atomic beam by giving the atoms initial velocities that obey a Maxwell-Boltzmann distribution at room temperature but are centered around 16 m/s (instead of 0 m/s).

To generate velocities with a Maxwell-Boltzmann distribution we exploit the fact that the Maxwell-Boltzmann speed distribution is the composition of three independent Gaussian distributions (corresponding to each cardinal direction). We generate the speed of each particle, v_{tot}:

$$v_{tot} = \sqrt{v_1^2 + v_2^2 + v_3^2} \tag{4.10}$$

where each of the v_i are chosen from a Gaussian distribution with $\mu = 0$ and $\sigma = \sqrt{\frac{k_B T}{m}}$. Then the $\hat{x}$-component of the atom's velocity, v_x, is chosen uniformly on the interval $[-v_{tot}, v_{tot}]$. The $\hat{y}$-component velocity, v_y, is then also chosen uniformly on the interval that will assure that the total speed cannot exceed v_{tot}: $[-\sqrt{v_{tot}^2 - v_x^2}, +\sqrt{v_{tot}^2 - v_x^2}]$. Finally, v_z is randomly chosen to be the positive or

negative of the "remaining" speed: $\pm\sqrt{v_{tot}^2 - v_x^2 - v_y^2}$.

To save computation time, the atoms are discarded if they have an initial total velocity $v_{tot} > 5v_c$, where $v_c \approx 20$m/s is the maximum capture velocity for the atoms calculated from a 1-dimensional analytical model [47]. For select parameter sets, we have checked this time-saving assumption against a version that simulates all atoms regardless of velocity and found no difference in the obtained results.

We numerically integrate the net acceleration on each atom (eqn. 4.5) by calculating the new velocity and position at each time step, dt, according to:

$$v_x = v_x + a_x dt \tag{4.11}$$

$$x = x + v_x dt + \frac{1}{2} a_x (dt)^2. \tag{4.12}$$

At each time step, any atoms that have left the simulation volume are discarded. The number of new atoms added is calculated by considering the average number of atoms that would leave the volume at each time step *assuming no radiation forces were present*:

$$n_{add} = \frac{n_{tot} dt}{\tau_{esc}}. \tag{4.13}$$

Here, n_{tot} is the total initial number of atoms in the simulation and τ_{esc} is the average escape time for atoms given by:

$$\tau_{esc} = \frac{w_{box}}{2v_{rms}} \tag{4.14}$$

where w_{box} is the linear dimension of the simulation volume and $v_{rms} = \sqrt{3k_B T/m}$. These new atoms are added with uniformly distributed positions along one of the (randomly) chosen simulation box edges and are given velocities that point inwards but correspond to a Maxwell-Boltzmann distribution (again discarding velocities greater than $5v_c$).

Every 100 time steps, we count the number of atoms with positions that are within $w_0/2$ of the origin. As a function of time, this sum produces a linear curve with a slope that corresponds to the loading rate of atoms being trapped by the MOT, L. The steady-state number of atoms confined by the MOT can then be calculated by including isotope abundance and the background collision and photoionization loss rates:

$$N_{ss} = \frac{fL}{n\sigma_c v_{rms} + \sigma_{ion} I_{tot} P(I,\delta)/\hbar\omega}. \tag{4.15}$$

Here, f is the relative abundance of the isotope of interest, $\sigma_c \approx 2 \times 10^{-17}$ cm^2 is the collision cross section, $\sigma_{ion} \approx 2 \times 10^{-16}$ cm^2 is the photoionization cross section of the ^{1}P$_1$ state, I_{tot} is the total laser intensity, and $P(I,\delta) = \frac{1}{2}\frac{s}{1+s+4\delta^2}$ is the probability of the atom being in the ^{1}P$_1$ state.

We have implemented this simulation using the Matlab programming language and we have used both Windows- and Unix-based workstations as well as a Unix-based cluster to perform the calculations. Full code is given in appendix C.

4.5 Simulation Results Compared to Experimental Data

To validate the accuracy of our computer model, we compare its predictions for steady-state trapped atom number with our experimental results.

A typical observation of the fluorescence growth from trapped atoms is shown in figure 4.8, allowing a determination of the steady-state number of atoms and the net loss rate, Γ, from the trap. An image of the fluorescence distribution from the trapped atoms is also shown, revealing a Gaussian-shaped atom cloud as expected from the temperature-limited density. The typical geometric mean rms radius of the MOT is 200 μm, with some dependence upon the magnetic field gradient, laser power and detuning. The largest MOT we have observed held approximately 3000

atoms, with a peak density of about 10^8 atoms/cm^3.

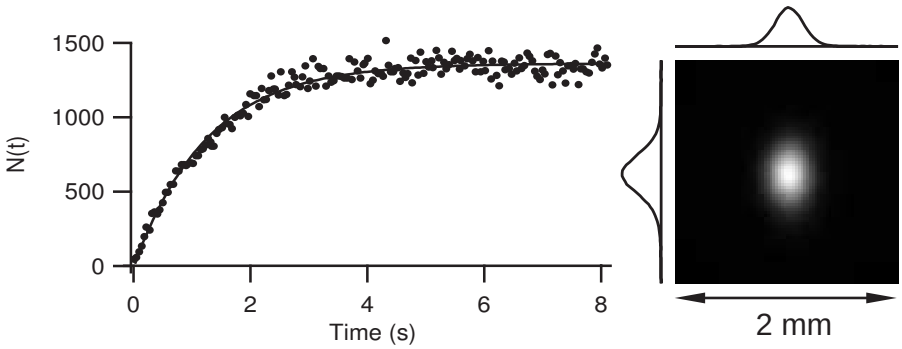

Figure 4.8: Typical loading curve and CCD image of Cd atoms confined in MOT. Left: Typical loading curve showing the buildup in the MOT fluorescence as a function of time. For this data set, the MOT parameters are: laser power $P = 1.45$ mW, beam waist $w = 1.25$ mm, detuning $\delta = -0.7$, and magnetic field gradient $B' = 500$ G/cm. The steady state MOT number is calculated from the fluorescence signal and for this data the buildup time is 1.5 sec. Right: MOT image taken with the camera for $N_{ss} = 1200$ atoms. The MOT parameters for this data set are $P = 1.45$ mW, $w = 2.5$ mm, $\delta = -0.7$, and $B' = 500$ G/cm. The integration time for the camera was 5 ms. A 2-D Gaussian fit to the image yields an rms radius of 200μm and a peak atom density of 10^8 atoms/cm^3.

Figure 4.9 shows the steady state number of atoms, N_{ss}, in the MOT vs. magnetic field gradient, B', for $w = 1.25$ mm, $\delta = -0.6$, and total power $P = 1.8$ mW. Under these conditions the maximum steady state number is observed at 500 G/cm. At this optimal field gradient, the Zeeman shift of the excited state levels at the edge of the laser beam is approximately one linewidth. Above this optimal value the steep magnetic field gradient shifts the atoms out of resonance with the laser beams, reducing the capture volume. At lower field gradients N_{ss} quickly decreases, presumably due to a lower trap depth resulting from an increased sensitivity to trapping parameters.

From the equipartition theorem we obtain a relation connecting the cloud radius and temperature: $\kappa r^2 = k_b T$, where r is the atomic cloud rms radius, k_b is Boltzmann's constant, T is the temperature in Kelvin, and κ is the trap spring

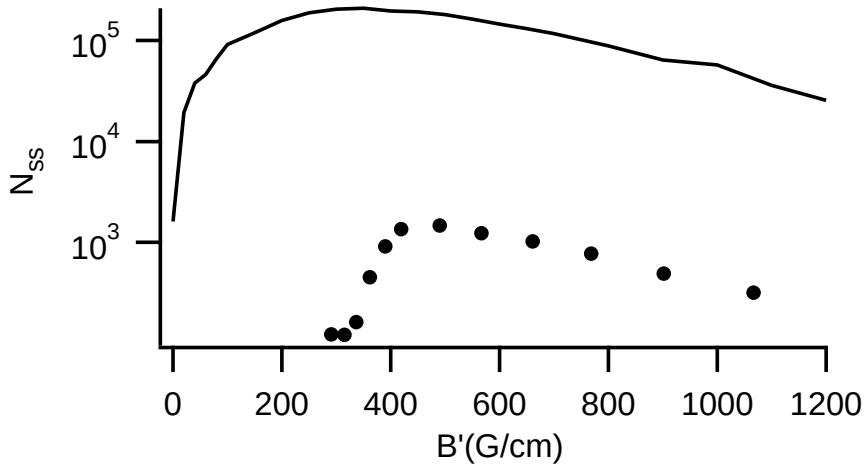

Figure 4.9: Steady-state MOT number vs. axial magnetic field gradient. Experimental observations (points) and 3-D model (solid line) are shown for $P = 0.8$ mW, $\delta = -0.6$, and $w = 2.5$ mm.

constant $\kappa = 8\mu_b ksB'\delta/(1+s+4\delta^2)$ [35]. In this expression, μ_b is the Bohr magneton, and $k = 2\pi/\lambda$ is the wavenumber. Replacing T with the Doppler temperature, $T_D = \hbar\gamma(1+s+4\delta^2)/(8k_b|\delta|)$, gives a relation between the temperature-limited cloud radius and the magnetic field gradient:

$$r = \sqrt{\frac{\hbar\gamma(1+s+4\delta^2)^3}{64\mu_b\delta^2 ksB'}}. \tag{4.16}$$

Figure 4.10 shows the MOT rms radius vs. magnetic field gradient; as expected from equation 4.16, the cloud gets smaller as B' increases. The MOT diameter is roughly 5 times larger than what Doppler theory predicts. Similar results were found in Sr, where the MOT temperature exceeded the expected Doppler temperature [62].

The dependence of the steady-state number of trapped atoms on MOT detuning and laser power is shown in figures 4.11 and 4.12. In both figures, the experimental data is plotted along with the 1-D and 3-D theoretical predictions. The observed number of trapped atoms is 1-2 orders of magnitude below predictions, likely due to alignment imperfections and intensity imbalances not included in the models. Figure

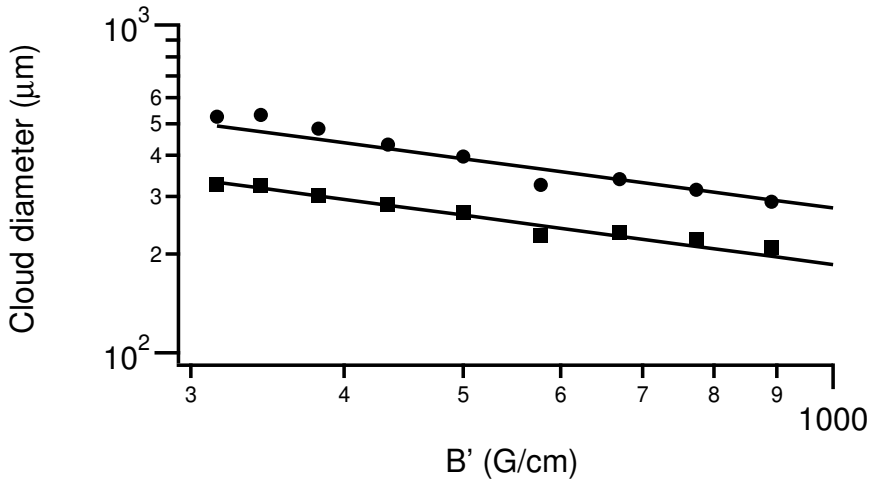

Figure 4.10: MOT cloud rms diameter vs. B'. Parameters are: $P = 0.8$ mW, $\delta = -0.6$, and $w = 2.5$ mm. A characterization is provided by the longest (circles) and shortest (squares) rms size of the elliptical MOT. The diameter is about 5 times larger than what Doppler theory predicts. The solid lines show the $(B')^{-1/2}$ dependence expected from eqn. 4.16.

4.13 shows how the measured atom cloud size decreases as the MOT laser power is increased (at a fixed beam waist), as expected from equation 4.16.

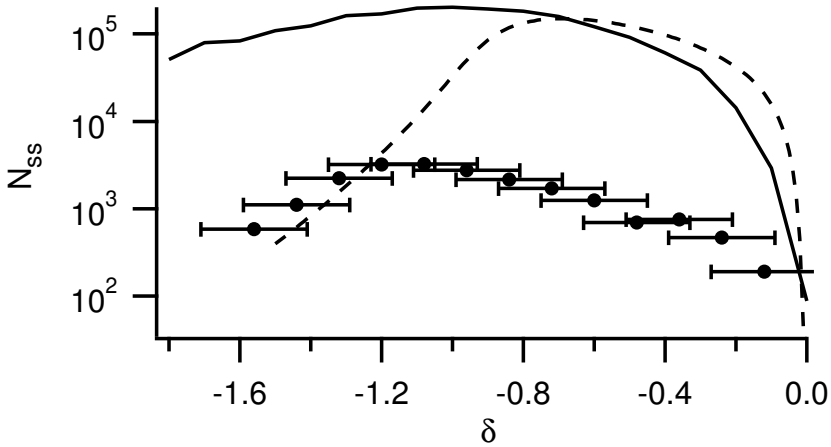

Figure 4.11: Observed steady-state atom number vs. detuning (δ). Experimental observations (points) along with the 1-D (dotted line) and 3-D (solid line) models are shown for $P = 1.8$ mW, $B' = 500$ G/cm and $w = 2.5$ mm.

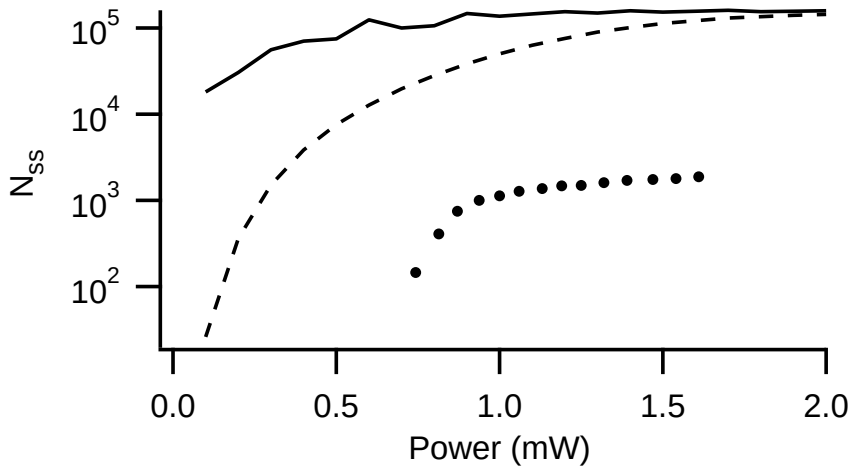

Figure 4.12: Observed steady-state atom number vs. power. Experimental observations (points) for $\delta = -0.7$, $B' = 500$ G/cm and $w = 2.5$ mm are shown with the 1-D (solid line) and 3-D (dotted line) models.

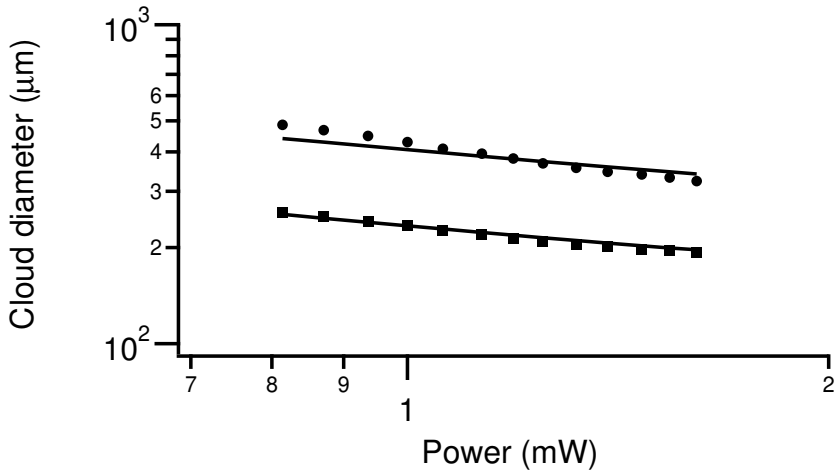

Figure 4.13: MOT cloud diameter vs. total MOT laser power. Parameters are: $\delta = -0.6$, $B' = 500$ G/cm and $w = 2.5$ mm. The solid lines show the expected dependence of the MOT diameter on power from eqn. 4.16.

CHAPTER V

Conclusion

5.1 Summary of Findings

In this thesis we have described a rigorous theory for trapped ion qubit state detection and experimentally verified this detection mechanism using Cd^+ (chapter II). We have constructed, tested, and utilized a scalable-geometry ion trap capable of switching the physical arrangement of ion crystals for use with quantum algorithms and simulations requiring larger numbers of ionic qubits (chapter III). And finally, we have characterized the first confinement of neutral Cd ions using magneto-optical trapping techniques to allow for detectable interactions between neutral and ionic Cd (chapter IV).

While not exhaustive, the following sections outline possible extensions of this work and some significant questions in this field.

5.2 Future Improvements

5.2.1 Multi-ion Detection As discussed in sec. 2.6, the current multi-ion detection fidelity of $\sim$ 98% is highly efficient, but improvements in light collection and/or CCD quantum efficiency would be necessary to increase the fidelity to perform fault-tolerant quantum computing with a reasonable number of qubits. In addition, the CCD total readout time of $\sim$ 15 ms is much longer than a typical gate time of

$\tau_{gate} \approx 100\mu$s, limiting the CCD's effectiveness for algorithms with steps conditional upon state detection (such as quantum error-correction [22] or the quantum Fourier transform [20]).

Fortunately, both limitations are ultimately technical. Current state-of-the-art unclassified CCDs operating in the near-IR can produce readout speeds of ~ 10 MHz per pixel or ~ 2.5 μs per ion ROI with quantum efficiencies of $\sim 60\%$. With these types of performance characteristics, employing CCDs for simultaneous multiple ion detection in feedback algorithms will be practical and efficient. Note that the fundamental limit on detection speed is given by the lifetime of the excited state: $\tau = \frac{2\pi}{\gamma}$. Thus, with high-efficiency light collection, the state detection time for Cd^+ could be as short as $\sim 50 - 200$ ns.

Large-scale ion trap arrays have been proposed [23, 85] and small, scalable traps have been successfully demonstrated using microfabrication techniques [86, 87]. Integrating multiple qubit detection via the CCD with these traps would produce a highly scalable qubit processing architecture.

5.2.2 Multi-zone Trap While we have successfully performed controlled shuttling of two ions in our multi-zone trap (including swapping the physical order of those two ions in a trapping zone), further experiments are possible with this current trap and with future improvements to the trap design and construction.

Of critical interest is the vibrational heating associated with storage and shuttling in this trap. Certainly shuttling adds kinetic energy to the ion, but to what extent and what techniques might minimize this heating remain open questions.

Once the heating rate is addressed, one could imagine using high-fidelity, two-ion entanglement to successively entangle multiple ions. As a possible idea, we could serially trap and entangle pairs of ions in a single trapping location before shuttling

one of these ions to a holding area and entangling a new ion with one of the previous qubits. Thus, we would build up entanglement to a large number of ions with the number limited by the combined fidelity of entangling and shuttling coupled with the need to perform the overall operation in a time that does not allow for significant heating of each ion's vibrational state. This multi-particle entanglement would be equally useful for performing a quantum algorithm or a quantum simulation.

The most important future improvement to trap design would be in trap fabrication and assembly techniques. Using hand-construction and assembly techniques for a trap with 49 electrodes was at the edge of reasonable technical and logistical expertise. In the future, using semi-conductor fabrication techniques for patterning and electrically shielding the trap electrodes would make for a truly scalable approach to a multi-zone trap structure [86, 87]. One could also explore alternate junction geometries (such as "X", "Y", or "cross") which may prove more benficial for particular applications.

5.2.3 Neutral Atom Experiments The realization of a neutral Cd trap represents a significant technical achievement and already points in many directions for future study. As examples, consider that the long-lived $^3P_0$ state could be of interest for optical clocks [56] and the narrow linewidth of the $^1S_0$-$^3P_1$ transition (70 kHz) would allow for an extremely low cooling limit [62].

Furthermore, producing an odd-isotope, fermionic MOT would be a true stepping-stone to neutral/ion experiments (sec. 5.2.4).

To understand the difficulty in producing an odd-isotope MOT, note that in fig. 4.1b, the two excited hyperfine states for both ^{111}Cd and ^{113}Cd are separated by about 300 MHz, which is comparable to the natural linewidth of Cd. A laser tuned to the red of the upper hyperfine state ($F' = 3/2$) but to the blue of the lower

hyperfine state ($F' = 1/2$) may drive excessive transitions to the lower excited state, which could result in too much heating and prevent trapping. In addition, the optical transitions between the $F = 1/2$ ground states and $F' = 1/2$ excited states do not result in spatially dependent differential optical pumping by σ^+ and σ^- transitions, a necessary condition for a standard MOT. Similar results were reported for Yb, where much smaller or no MOT was observed for fermionic isotopes [63]. In our experiments it is possible that there is a very small fermionic MOT being formed but it is not resolvable from the background noise.

To produce a fermionic neutral Cd trap, it may be possible to laser cool and trap fermionic isotopes with a dichroic MOT [88]. Here, the cooling laser is tuned to the red of the lower hyperfine transitions ($F' = 1/2$) to provide the major scattering force for laser cooling and then a small fraction of the laser power is frequency shifted to the red of the upper hyperfine state (blue of the lower state). When this second laser beam is collimated with a smaller beam waist, and overlapped with the beam of the first color, the laser cooled atoms can be trapped in the MOT by driving the upper transitions ($F = 1/2 \rightarrow F' = 3/2$). Alternatively, one can work in a much higher magnetic field gradient to overwhelm the excited state hyperfine structure. In this Paschen-Bach regime, one will drive $J = 0 \rightarrow J = 1$ transitions to produce a MOT. Given a beam waist of 1.0 mm, the required field gradient for the MOT will be on the order of 10^4 G/cm, which can be realized by a pair of needle electromagnets [89]. The capture volume of the MOT will be much smaller, but this scheme may still be useful for single-atom MOT experiments. Another alternative is to use a higher laser power allowing one to tune to the red of both hyperfine states. With a larger detuning ($|\delta| \gg \delta_{hf}$) the optical excitation to the lower and upper manifolds is driven more evenly and can produce both cooling and trapping forces for the atoms.

5.2.4 MOT and Ion Experiment If one can reliably trap neutral Cd, then exploiting our expertise in controlling cold Cd ions would allow for the possibility of studying ultra-cold charge exchange collisions. One particularly exciting outcome of these studies might be the possible transfer of coherent information from an individual ion to an individual neutral atom. A possible experiment is to prepare the ion in a coherent superposition of the hyperfine qubit states and then allow the ion to undergo an ultracold charge exchange with a nearby neutral atom. This results in the charge neutralization of the ion, but could also leave some of the previously prepared quantum information intact in the nucleus. This could allow quantum information to be carried by pure nuclear spins with very little interaction with the environment. Subsequent coherent charge exchange with another ion would then allow the nuclear quantum information to be manipulated and processed using conventional ion trap techniques.

In order to controllably interact ions with neutral atoms we need to be able to produce a MOT that is co-located near an ion trap. While theoretically manageable, the technical difficulties of this idea remain formidable. As an example of some of the difficulties, consider the neutral trapping laser beam size: larger beams allow for more stability and significantly easier alignment, but ion traps must be relatively small in order to produce the required electric trapping fields. Scatter of the MOT beams on the ion trap not only scrambles their polarization and thereby destabilizes the trap, but the scatter also makes detection of the ions with the CCD extremely difficult. Furthermore, technical difficulties in producing a strong magnetic field gradient mean that the ion imaging lens must be placed so far away from the ion that the ion's diffraction-limited size is < 1 pixel on the CCD making even background-free imaging challenging.

Significant time, energy, and expertise has gone into attempts to produce and image ions co-located with a MOT, but thus far we have not been successful.

If one could trap neutral and ionic atoms in the same region then some experiments become immediately available. One possible experiment would be to simply characterize the interaction between neutral and ionic atoms by trapping an ion of one species and a neutral trap filled with a different species. As an example, we could produce a ^{112}Cd MOT which via photo-ionization would produce $^{112}Cd^{+}$ ions and we could trap one of these in our ion trap and cool it with an appropriately tuned doppler-cooling laser. After moving the ion away from the MOT trapping region, we could then blue-shift the MOT trapping laser to confine ^{114}Cd neutral atoms. Then, while watching the ion on the CCD, we could controllably move the ion closer to the MOT and observe when it undergoes a charge-exchange collision with a neutral atom. At the end of this charge-exchange there will still be one neutral atom and one ion, but their isotopes will be reversed from the initial situation and thus the $^{112}Cd^{+}$-tuned Doppler-cooling laser will be blue of the $^{114}Cd^{+}$ resonance so the new ion will disappear to indicate that it has undergone a charge-exchange. We could repeat this experiment multiple times to determine the probability of undergoing charge-exchange as a function of distance between the ion and the MOT center. We predict that this curve would closely mirror the spatial atom density within the MOT, but it would be a direct measurement of this charge-exchange.

APPENDICES

APPENDIX A

Frequency Doubling Conversion Efficiency

Frequency doubling or second-harmonic generation (SHG) exploits the non-linear susceptibility of a dielectric material ($\chi^{(2)}$) to produce light at frequency 2ω from input radiation at frequency ω. The key idea behind this SHG is that one needs to create this doubled light in phase throughout the material such that it adds to the 2nd harmonic light that has already been created. In this appendix we discuss the efficiency of converting blue radiation to UV light by exploiting the birefringence of β-BaB_2O_4 (BBO).

A.1 BBO & Phase-Matching

BBO is a negative uniaxial crystal meaning that is has only one axis along which light is not doubly refracted (namely there is one optical axis) and its extraordinary refractive index is less than its ordinary refractive index (hence "negative"). Ordinary rays are defined as those rays with light polarized perpendicular to the plane containing the propagation vector ($\mathbf{k}$) and the optic axis ($\mathbf{z}$) (see figure A.1). Extraordinary rays are polarized in the plane containing $\mathbf{k}$ and $\mathbf{z}$.

Recall that the idea is to produce light at 2ω that is in phase with the propagating incoming light at ω, so we need to set up our system such that $\Delta k = 2k_1 - k_2 = 2n_\omega\omega/c - n_{2\omega}2\omega/c = 0$. Since BBO is a negative uniaxial crystal, for SHG we want

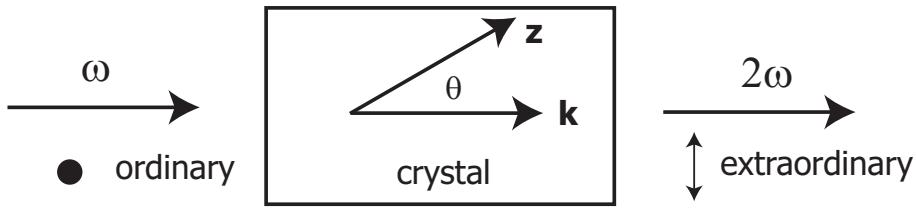

Figure A.1: Generalized diagram showing the orientations of the crytal axes and the ensuing definitions of ordinary and extraordinary rays.

the fundamental to be the ordinary wave and the harmonic to be the extraordinary ray. Thus, we want $n_e(2\omega) = n_o(\omega)$ [90]:

$$\sin^2\theta = \frac{\frac{1}{n_o(\omega)^2} - \frac{1}{n_o(2\omega)^2}}{\frac{1}{n_e(2\omega)^2} - \frac{1}{n_o(2\omega)^2}} \tag{A.1}$$

which tells us how to orient the crystal to achieve the phase-matching condition. Note that this equation also shows why choosing the right crystal is important: if the normal dispersion (the numerator) is larger than the birefringence (the denominator) then the fraction is greater than 1 and no orientation will exist to produce phase-matching.

For BBO, the indices of refraction are approximately given by the Sellmeier equations:

$$\begin{aligned} n_o^2(\lambda) &= 2.7359 + 0.01878/(\lambda^2 - 0.01822) - 0.01354\lambda^2 \\ n_e^2(\lambda) &= 2.3753 + 0.01224/(\lambda^2 - 0.01667) - 0.01516\lambda^2 \end{aligned} \tag{A.2}$$

where λ is measured in μm. Therefore, if we want to convert 457 nm light to 229 nm light we would want the crystal angle to be: $\theta = 61.33°$ (crystal companies quote $\theta = 61.4°$ with the difference attributable to the Sellmeier equation approximation).

When θ is different from 0° or 90° there will be beam walk-off because the propagation vector, **k**, is not parallel to the Poynting vector, **S**. This walk-off limits the crystal length over which one can achieve significant SHG. Periodic-poling of the

material could solve this walk-off issue, but that discussion is beyond the present scope.

A.2 SHG Conversion Efficiency

If we ignore walk-off, we can write an efficiency of non-linear conversion given by [91]:

$$\eta \equiv \frac{P_{2\omega}}{P_\omega} = K \frac{P_\omega}{w_0^2} l^2 \tag{A.3}$$

where P_ω ($P_{2\omega}$) is the power at the fundamental (harmonic) frequency, w_0 is the beam waist at the center of the crystal, and l is the effective length of the crystal. The "gain", K, is given by:

$$K = \frac{2\omega^2 d_{\text{eff}}^2}{\epsilon_0 n_1^2 n_2 c^3 \pi} \tag{A.4}$$

where d_{eff} is the 2nd order polarization coefficient of the crystal, ϵ_0 is the permittivity of free space, n_1 (n_2) is the index of refraction at the fundamental (harmonic) frequency, and c is the speed of light. The polarization coefficient (d_{eff}) is itself a function of the wavelength and for type I phase matching we have:

$$d_{\text{eff}} = d_{31} \sin\theta + d_{11} \cos\theta. \tag{A.5}$$

Here θ is the crystal angle from eqn. A.1 and $d_{31} = 2.55$ pm/V and $d_{11} = 0.025$ pm/V are the nonlinear optical susceptibilities of BBO.

Thus, we can combine eqns. A.3 and A.4 to write the 2nd harmonic output power as a function of input power:

$$P_{2\omega} = \frac{2\omega^2 d_{\text{eff}}^2 P_\omega^2 l^2}{\epsilon_0 n_1^2 n_2 c^3 \pi w_0^2}. \tag{A.6}$$

Experimentally, we focus the incoming beam to a waist of $w_0 \approx 200$ μm and we have an effective crystal length of $l \approx 5$ mm, but note that if we simply apply our

$\sim$ 150 mW of cw blue (λ = 457 nm) light to the crystal then eqn. A.6 predicts P_{out} = 260 nW. In fact, we must use a confocal build-up cavity around the BBO crystal such that the circulating power at the fundamental is increased by the cavity build-up factor ($Q = \frac{\mathcal{F}}{\pi} = \frac{\text{FSR}}{\pi\text{FWHM}}$). With $Q \approx 150$, we find that our predicted 229 nm output power is $P_{\text{out}} = 5.9$ mW. In practice, we are typically able to produce $\sim$ 2.5 mW output power from an input power of $\sim$ 150 mW, with the difference from theory being of unknown origin.

As illustrated in figure A.2, the doubling efficiency of BBO depends strongly on the wavelength of the fundamental radiation. Examining the wavelength dependencies of eqn. A.6 we can see that output power from BBO exhibits a maximum (rather than monotonically increasing or decreasing) because while increasing wavelength yields increasing d_{eff} (and similarly decreasing n_1 and n_2), ω decreases and its inverse decay eventually outweighs the other effects. Note also that doubling using BBO cuts off at $\lambda \approx 410$ nm because the necessary angle to produce phase-matching (eqn. A.1) exceeds 90°.

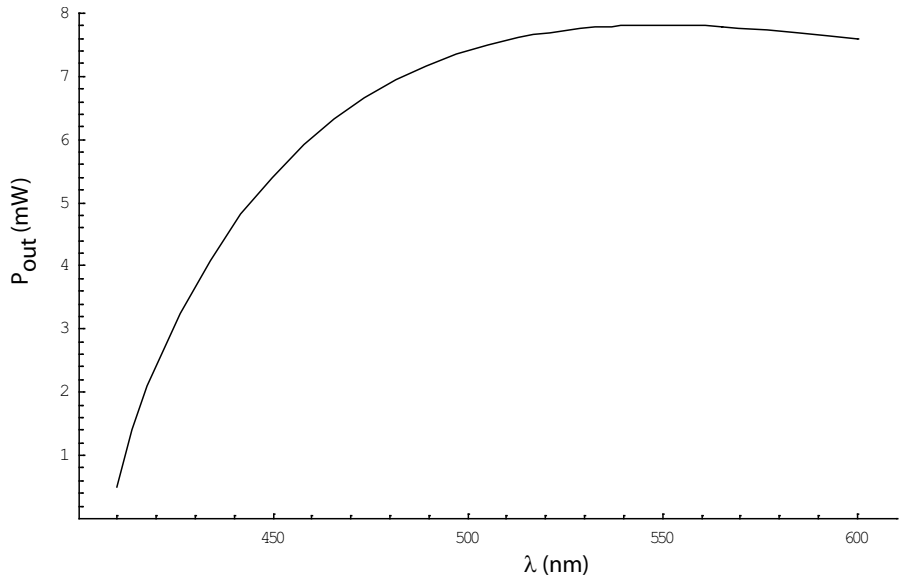

Figure A.2: Doubling efficiency of BBO as a function of fundamental wavelength. Parameters, from the text, are: $Q = 150$, $w_0 = 200$ μm, $l = 5$ mm, and $P_{\text{in}} = 150$ mW.

APPENDIX B

Laser Beam Pair Intensity Imbalance

Note that laser intensity imbalance between the counter-propagating beam pairs does not directly preclude formation of a stable trap, but instead leads to MOT formation misaligned from the magnetic field null. If we consider the one-dimensional case (here along $\hat{z}$) of two counter-propagating beams then the MOT will be formed where the net restoring force on the atoms is zero:

$$\frac{\hbar k\gamma}{2}\frac{s_+}{1+s+\frac{4}{\gamma^2}(\Delta+\frac{\mu_B g_F B' z}{\hbar})^2} = \frac{\hbar k\gamma}{2}\frac{s_-}{1+s+\frac{4}{\gamma^2}(\Delta-\frac{\mu_B g_F B' z}{\hbar})^2}. \tag{B.1}$$

If we define a relative intensity imbalance $\epsilon \equiv \frac{s_+}{s_-} - 1$, then we can simplify this expression to

$$\frac{1+\epsilon}{1+s+\frac{4}{\gamma^2}(\Delta+\frac{\mu_B g_F B' z}{\hbar})^2} = \frac{1}{1+s+\frac{4}{\gamma^2}(\Delta-\frac{\mu_B g_F B' z}{\hbar})^2}. \tag{B.2}$$

We wish to solve for the position, $z = z_0$, where eqn. B.2 is satisfied. Algebraic simplification leads to:

$$\frac{4\epsilon\mu_B^2 g_F^2 B'^2}{\hbar^2\gamma^2}z^2 - \frac{16\delta\mu_B g_F B'(1+\epsilon/2)}{\hbar\gamma^2}z - \epsilon\left(1+s+\frac{4\delta^2}{\gamma^2}\right) = 0. \tag{B.3}$$

We can then use the quadratic formula to obtain the equilibrium position of the MOT:

$$z_0 = \frac{4\hbar\delta(1+\epsilon/2) + \hbar\gamma\sqrt{(1+s)\epsilon^2 + \frac{8\delta^2}{\gamma^2}(2+2\epsilon+\epsilon^2)}}{2\mu_B g_F B'\epsilon} \tag{B.4}$$

where we have ignored the other (non-physical) root.

APPENDIX C

MOT Simulation Code

```
%This version of the program has all the necessary features to look for a
%MOT, including repopulating the simulation region with new particles as
%time goes on. It simulates the magnetic field as a quadrupole and allows for a power imbalance.
%It also includes a psuedo-atomic beam of atoms.

function [sum_center] = MOT_simulation(total_power, w0, B_gradient, laser_detuning, imbalance)
%Note that the function variables are in SI units, except for
%laser_detuning which is defined as a fraction of gamma and
%imbalance which is a vector in fractional units.

c = 2.998*10^8; %speed of light
boltzmann = 1.38*10^(-23); %Boltzmann constant
mass_proton = 1.67*10^(-27); %mass in kg
hbar = 1.055*10^(-34);
bohr_magneton = 9.27 * 10^(-24); %Bohr magneton
g_lande = 1; %Lande g-factor
mass = 112*mass_proton;
lambda = 228.8 * 10^(-9); %wavelength in meters
k = 2*pi/lambda; %wavenumber in 1/m
gamma = 2*pi*95*10^6; %radiative linewidth
I_sat = pi*2*pi*hbar*c*gamma/(3*(lambda)^3); %saturation intensity
scatter_const = hbar*k*gamma/(2*mass); %numerical constant in front of scattering eqn
mag_const = bohr_magneton*g_lande/hbar; %numerical constant in front of mag-field shift

%This section gives simulation numerical parameters
dt = 200/(gamma/2);
tfinal = (1*10^5)*dt;

%This section is where you can change the physical parameters
Pressure = 2*10^(-12) * 133.3; %pressure in Pascals
Temp = 293; %temperature in Kelvin
laser_detuning = laser_detuning*gamma; %negative detuning gives cooling
box_width = 3*w0;
Volume = (2*box_width)^3;
num_particles = round(Pressure*Volume/(boltzmann*Temp));

I_beam = (2*total_power/6)/(pi*w0^2); %single-beam intensity
I_x = imbalance(1)*I_beam;
I_y = imbalance(2)*I_beam;
I_z = imbalance(3)*I_beam;

v_sd=sqrt(boltzmann*Temp/mass);
t_escape = box_width / (sqrt(3)*v_sd); %the avg escape time for half the particles
num_add = round(num_particles*dt/(2*t_escape)); %the number of particles to add per time step

vel_cutoff = 100;

velocity_matrix=ones(num_particles,3);
```

```
flag=0;
for j=1:num_particles
vel_total = sqrt(normrnd(0,v_sd)^2 + normrnd(0,v_sd)^2 + normrnd(0,v_sd)^2);
if vel_total <= vel_cutoff
flag=flag+1;
velocity_matrix(flag,1) = unifrnd(-vel_total,vel_total);
temp = sqrt(vel_total^2 - velocity_matrix(flag,1)^2);
velocity_matrix(flag,2) = unifrnd(-temp,temp);
velocity_matrix(flag,3) = (2*randint - 1)*sqrt(vel_total^2 ...
- velocity_matrix(flag,1)^2 - velocity_matrix(flag,2)^2);
velocity_matrix(flag,1) = velocity_matrix(flag,1) + 15;
velocity_matrix(flag,2) = velocity_matrix(flag,2) + 5;
end
end

extra_factor = 0.5; %buffer factor to add on to position and velocity matrices
velocity_matrix = velocity_matrix(1:((1+extra_factor)*flag),:);

position_matrix = unifrnd(-box_width,box_width,size(velocity_matrix));

sum_center = []; %initialize the count of particles in the center of our beams

for t=0:dt:tfinal,
acceleration_matrix = MOT_accel(position_matrix, velocity_matrix);
%calculates the acceleration on each particle
velocity_matrix = velocity_matrix + acceleration_matrix*dt;
%updates the velocities for each atom
position_matrix = position_matrix + dt*(velocity_matrix + 0.5*acceleration_matrix*dt);
        %updates the positions for each atom

if mod(t/dt,100)==0 %update number of particles in center every 100th iteration
sum_center = [sum_center; t, sum((abs(position_matrix(:,1)) <= 0.5*w0) &...
(abs(position_matrix(:,2)) <= 0.5*w0) &...
(abs(position_matrix(:,3)) <= 0.5*w0))];
end

%now we want to stop simulating atoms that have left the simulation volume by removing them
j=1;
while j<=flag
if (abs(position_matrix(j,1))>box_width) || (abs(position_matrix(j,2))>box_width) ...
|| (abs(position_matrix(j,3))>box_width)
position_matrix(j,:)=position_matrix(flag,:);
velocity_matrix(j,:)=velocity_matrix(flag,:);
flag=flag-1;
else
j=j+1;
end
end


%now add atoms at the box edges while making sure that they go inwards
for j=1:num_add
vel_total = sqrt(normrnd(0,v_sd)^2 + normrnd(0,v_sd)^2 + normrnd(0,v_sd)^2);
if vel_total <= vel_cutoff
flag=flag+1;
velocity_matrix(flag,1) = unifrnd(-vel_total,vel_total);
temp = sqrt(vel_total^2 - velocity_matrix(flag,1)^2);
velocity_matrix(flag,2) = unifrnd(-temp,temp);
velocity_matrix(flag,3) = (2*randint - 1)*sqrt(vel_total^2 ...
- velocity_matrix(flag,1)^2 - velocity_matrix(flag,2)^2);
velocity_matrix(flag,1) = velocity_matrix(flag,1) + 15;
velocity_matrix(flag,2) = velocity_matrix(flag,2) + 5;
position_matrix(flag,:) = unifrnd(-box_width,box_width,1,3);
edge = randint(1,1,[1,6]);
if edge==1
position_matrix(flag,1) = -box_width;
velocity_matrix(flag,1) = abs(velocity_matrix(flag,1));
elseif edge==2
```

```
position_matrix(flag,1) = box_width;
velocity_matrix(flag,1) = -abs(velocity_matrix(flag,1));
elseif edge==3
position_matrix(flag,2) = -box_width;
velocity_matrix(flag,2) = abs(velocity_matrix(flag,2));
elseif edge==4
position_matrix(flag,2) = box_width;
velocity_matrix(flag,2) = -abs(velocity_matrix(flag,2));
elseif edge==5
position_matrix(flag,3) = -box_width;
velocity_matrix(flag,3) = abs(velocity_matrix(flag,3));
else
position_matrix(flag,3) = box_width;
velocity_matrix(flag,3) = -abs(velocity_matrix(flag,3));
end %if statements for picking new particle edge and velocity
end %if statement for velocity cutoff
end %for loop for adding particles

end %atom position iterations


function accel_mat = MOT_accel(position_matrix, velocity_matrix)
%sub-function to calculate the acceleration on each particle
%returns an n-by-3 matrix corresponding to the 3 different
%directions (x,y,z)

sat_x=sx(position_matrix);
sat_y=sy(position_matrix);
sat_z=sz(position_matrix);
B_mat=B_mag(position_matrix);
sat_tot = [2*sat_x + 2*sat_y + 2*sat_z,...
2*sat_x + 2*sat_y + 2*sat_z, 2*sat_x + 2*sat_y + 2*sat_z];
accel_mat(:,1) = (scatter_const*2*sat_x) .* ...
(imbalance(4)*sum(pol_x_plus(position_matrix)./(1+sat_tot+...
(2*delta_plus(velocity_matrix(:,1))/gamma).^2),2) ...
- (1-imbalance(4))*sum(pol_x_minus(position_matrix)./...
(1+sat_tot+(2*delta_minus(velocity_matrix(:,1))/gamma).^2),2));
accel_mat(:,2) = (scatter_const*2*sat_y) .* ...
(imbalance(5)*sum(pol_y_plus(position_matrix)./(1+sat_tot+...
(2*delta_plus(velocity_matrix(:,2))/gamma).^2),2) ...
- (1-imbalance(5))*sum(pol_y_minus(position_matrix)./...
(1+sat_tot+(2*delta_minus(velocity_matrix(:,2))/gamma).^2),2));
accel_mat(:,3) = (scatter_const*2*sat_z) .* ...
(imbalance(6)*sum(pol_z_plus(position_matrix)./(1+sat_tot+...
(2*delta_plus(velocity_matrix(:,3))/gamma).^2),2) ...
- (1-imbalance(6))*sum(pol_z_minus(position_matrix)./...
(1+sat_tot+(2*delta_minus(velocity_matrix(:,3))/gamma).^2),2));

function sat_x = sx(position)
%returns an n-length column vector
sat_x = (I_x/I_sat) .* exp((-2*(position(:,2).^2 + position(:,3).^2))./(w0^2));
end %sx

function sat_y = sy(position)
%returns an n-length column vector
sat_y = (I_y/I_sat) .* exp((-2*(position(:,1).^2 + position(:,3).^2))./(w0^2));
end %sy

function sat_z = sz(position)
%returns an n-length column vector
sat_z = (I_z/I_sat) .* exp((-2*(position(:,1).^2 + position(:,2).^2))./(w0^2));
end %sz

function d_plus = delta_plus(velocity)
%subfunction to calculate the positive-going detuning for each atom
%note that the function outputs an n-by-3 matrix corresponding to the
%detuning for the 3 polarizations (sig-,pi,sig+)
temp_mat=mag_const*B_gradient*B_mat*[-1,0,1];
```

```
d_plus = laser_detuning + [-k*velocity-temp_mat(:,1),...
-k*velocity-temp_mat(:,2), -k*velocity-temp_mat(:,3)];
end %delta_plus

function d_minus = delta_minus(velocity)
%subfunction to calculate the negative-going detuning for each atom
%note that the function outputs an n-by-3 matrix corresponding to the
%detuning for the 3 polarizations (sig-,pi,sig+)
temp_mat=mag_const*B_gradient*B_mat*[-1,0,1];
d_minus = laser_detuning + [k*velocity-temp_mat(:,1),...
k*velocity-temp_mat(:,2), k*velocity-temp_mat(:,3)];
end %delta_minus

function mag_field = B_mag(position)
%this sub-function calculates the magnetic field strength
%it returns an n-length column vector
mag_field = sqrt(position(:,3).^2 + 0.25*(position(:,1).^2 + position(:,2).^2));
end %B_mag

function pol_prob = pol_x_plus(position)
%this function calculates the probabilities of transitions due to
%each polarization (sig-,pi,sig+) for the positive going x-beam
%it assumes that the x-direction beams are sig- polarized initially
%returns an n-by-3 matrix corresponding to the 3 polarizations
pol_prob(:,1) = (0.5*(1-0.5*position(:,1)./B_mat)).^2;
pol_prob(:,3) = (0.5*(1+0.5*position(:,1)./B_mat)).^2;
pol_prob(:,2) = 1-(pol_prob(:,1)+pol_prob(:,3));
end %pol_x_plus

function pol_prob = pol_x_minus(position)
%this function calculates the probabilities of transitions due to
%each polarization (sig-,pi,sig+) for the minus going x-beam
%it assumes that the x-direction beams are sig- polarized initially
%returns an n-by-3 matrix corresponding to the 3 polarizations
pol_prob(:,1) = (0.5*(1+0.5*position(:,1)./B_mat)).^2;
pol_prob(:,3) = (0.5*(1-0.5*position(:,1)./B_mat)).^2;
pol_prob(:,2) = 1-(pol_prob(:,1)+pol_prob(:,3));
end %pol_x_minus

function pol_prob = pol_y_plus(position)
%this function calculates the probabilities of transitions due to
%each polarization (sig-,pi,sig+) for the positive going y-beam
%it assumes that the y-direction beams are sig- polarized initially
        %returns an n-by-3 matrix corresponding to the 3 polarizations
pol_prob(:,1) = (0.5*(1-0.5*position(:,2)./B_mat)).^2;
pol_prob(:,3) = (0.5*(1+0.5*position(:,2)./B_mat)).^2;
pol_prob(:,2) = 1-(pol_prob(:,1)+pol_prob(:,3));
end %pol_y_plus

function pol_prob = pol_y_minus(position)
%this function calculates the probabilities of transitions due to
%each polarization (sig-,pi,sig+) for the minus going y-beam
%it assumes that the y-direction beams are sig- polarized initially
%returns an n-by-3 matrix corresponding to the 3 polarizations
pol_prob(:,1) = (0.5*(1+0.5*position(:,2)./B_mat)).^2;
pol_prob(:,3) = (0.5*(1-0.5*position(:,2)./B_mat)).^2;
pol_prob(:,2) = 1-(pol_prob(:,1)+pol_prob(:,3));
end %pol_y_minus

function pol_prob = pol_z_plus(position)
%this function calculates the probabilities of transitions due to
%each polarization (sig-,pi,sig+) for the positive going z-beam
%it assumes that the z-direction beams are sig+ polarized initially
%returns an n-by-3 matrix corresponding to the 3 polarizations
pol_prob(:,1) = (0.5*(1-position(:,3)./B_mat)).^2;
pol_prob(:,3) = (0.5*(1+position(:,3)./B_mat)).^2;
pol_prob(:,2) = 1-(pol_prob(:,1)+pol_prob(:,3));
end %pol_z_plus
```

```
function pol_prob = pol_z_minus(position)
%this function calculates the probabilities of transitions due to
%each polarization (sig-,pi,sig+) for the minus going z-beam
%it assumes that the z-direction beams are sig+ polarized initially
%returns an n-by-3 matrix corresponding to the 3 polarizations
pol_prob(:,1) = (0.5*(1+position(:,3)./B_mat)).^2;
pol_prob(:,3) = (0.5*(1-position(:,3)./B_mat)).^2;
pol_prob(:,2) = 1-(pol_prob(:,1)+pol_prob(:,3));
end %pol_z_minus

end %MOT_accel

end %MOT_simulation
```

BIBLIOGRAPHY

BIBLIOGRAPHY

[1] M. A. Nielsen and I. L. Chuang. *Quantum Computation and Quantum Information*. Cambridge University Press, Cambridge, UK, 3rd edition, 2000.

[2] R. Raussendorf and H. J. Briegel. A one-way quantum computer. *Phys. Rev. Lett.*, 86:5188, 2001.

[3] L.-M. Duan and R. Raussendorf. Efficient quantum computation with probabilistic quantum gates. *Phys. Rev. Lett.*, 95:080503, 2005.

[4] P. W. Shor. Algorithm for fast factoring. *SIAM J. Comp.*, 26:1484, 1997.

[5] L. K. Grover. Quantum mechanics helps in searching for a needle in a haystack. *Phys. Rev. Lett.*, 79(2):325–328, Jul 1997.

[6] R. P. Feynman. Simulating physics with computers. *Int. J. Th. Phys.*, 21(6/7):467–488, 1982.

[7] T. Rosenband, D. B. Hume, P. O. Schmidt, C. W. Chou, A. Brusch, L. Lorini, W. H. Oskay, R. E. Drullinger, T. M. Fortier, J. E. Stalnaker, S. A. Diddams, W. C. Swann, N. R. Newbury, W. M. Itano, D. J. Wineland, and J. C. Bergquist. Frequency ratio of al+ and hg+ single-ion optical clocks; metrology at the 17th decimal place. *Science*, 319:1808, 2008.

[8] J. S. Bell. On the einstein-podolsky-rosen paradox. *Physics*, 1:195, 1964.

[9] M. A. Rowe, D. Kielpinski, V. Meyer, C. A. Sackett, W. M. Itano, C. Monroe, and D. J. Wineland. Experimental violation of a bell's inequality with efficient detection. *Nature*, 409:791, 2001.

[10] D. L. Moehring, M. J. Madsen, B. B. Blinov, and C. Monroe. Experimental bell inequality violation with an atom and a photon. *Phys. Rev. Lett.*, 93:090410, 2004.

[11] R. S. Van Dyck, Jr., P. B. Pschwinberg, and H. G. Dehmelt. New high-precision comparison of electron and positron g factors. *Phys. Rev. Lett.*, 59:26–29, 1987.

[12] M. E. Poitzsch, J. C. Bergquist, W. M. Itano, and D. J. Wineland. Cryogenic linear ion trap for accurate spectroscopy. *Rev. Sci. Inst.*, 67:129, 1996.

[13] M. Acton, K-A Brickman, P. C. Haljan, P. J. Lee, L. Deslauriers, and C. Monroe. Near-perfect simultaneous measurement of a qubit register. *QIC*, 6:465, 2006.

[14] W. Nagourney, J. Sandberg, and H. Dehmelt. Shelved optical electron amplifier: observation of quantum jumps. *Phys. Rev. Lett.*, 56:2797, 1986.

[15] Th. Sauter, W. Neuhauser, R. Blatt, and P. E. Toschek. Observation of quantum jumps. *Phys. Rev. Lett.*, 57:1696, 1986.

[16] J. C. Bergquist, R. G. Hulet, W. M. Itano, and D. J. Wineland. Observation of quantum jumps in a single atom. *Phys. Rev. Lett.*, 57:1699, 1986.

[17] R. Blatt and P. Zoller. Quantum jumps in atomic systems. *Eur. J. Phys.*, 9(4):250 – 6, 1988.

[18] C. F. Roos, G. P. T. Lancaster, M. Riebe, H. Häffner, W. Hänsel, S. Gulde, C. Bechner, J. Eschner, F. Schmidt-Kaler, and R. Blatt. Bell states of atoms with ultralong lifetimes and their tomographic state analysis. *Phys. Rev. Lett.*, 92:220402, 2004.

[19] P. C. Haljan, P. J. Lee, K-A. Brickman, M. Acton, L. Deslauriers, and C. Monroe. Entanglement of trapped-ion clock states. *Phys. Rev. A*, 72(6):062316, 2005.

[20] J. Chiaverini, J. Britton, D. Leibfried, E. Krill, M. D. Barrett, R. B. Blakestad, W. M. Itano, J. D. Jost, C. Langer, R. Ozeri, T. Schaetz, and D. J. Wineland. Implementation of the semiclassical quantum fourier transform in a scalable system. *Science*, 308(5724):997–1000, May 2005.

[21] K.-A. Brickman, P. C. Haljan, P. J. Lee, M. Acton, L. Deslauriers, and C. Monroe. Implementation of grover's quantum search algorithm in a scalable system. *Phys. Rev. A*, 72:050306, 2005.

[22] J. Chiaverini, D. Leibfried, T. Schaetz, M. D. Barrett, R. B. Blakestad, J. Britton, W. M. Itano, J. D. Jost, E. Knill, C. Langer, R. Ozeri, and D. J. Wineland. Realization of quantum error correction. *Nature*, 432:602, 2004.

[23] D. Kielpinski, C. Monroe, and D. J. Wineland. Architecture for a large-scale ion-trap quantum computer. *Nature*, 417:709–711, 2002.

[24] M. A. Rowe, A. Ben Kish, B. L. DeMarco, D. Leibfried, V. Meyer, J. Britton, J. Hughers, W. M. Itano, B. M. Jelenkovic, C. Langer, T. Rosenband, and D. J. Wineland. Transport of quantum states and separation of ions in a dual rf ion trap. *QIC*, 2:257–271, 2002.

[25] W. K. Hensinger, S. Olmschenk, D. Stick, D. Hucul, M. Yeo, M. Acton, L. Deslauriers, C. Monroe, and J. Rabchuk. T-junction ion trap array for two-dimensional ion shuttling, storage, and manipulation. *Appl. Phys. Lett.*, 88(3):034101, 2006.

[26] C. F. Roos, Th. Zeiger, H. Rohde, H.C. Nägerl, J. Eschner, D. Leibfried, F. Schmidt-Kaler, and R. Blatt. Quantum state engineering on an optical transition and decoherence in a paul trap. *Phys. Rev. Lett.*, 83:4713, 1999.

[27] P. A. Barton, C. J. S. Donald, D. M. Lucas, D. A. Stevens, A. M. Steane, and D. N. Stacey. Measurement of the lifetime of the 3d $^2d_{5/2}$ state in $^{40}ca^+$. *Phys. Rev. A*, 62:032503, 2000.

[28] Chr. Wunderlich, Th. Hannemann, T. Körber, H. Häffner, Ch. Roos, W. Hänsel, R. Blatt, and F. Schmidt-Kaler. Robust state preparation of a single trapped ion by adiabatic passage. *J. Mod. Opt.*, 54:1541, 2007.

[29] M. J. McDonnell, J.-P. Stacey, S. C. Webster, J. P. Home, A. Ramos, D. M. Lucas, D. N. Stacey, and A. M. Steane. High-efficiency detection of a single quantum of angular momentum by suppression of optical pumping. *Phys. Rev. Lett.*, 93:153601, 2004.

[30] J. C. Bergquist, U. Tanaka, R. E. Druillinger, W. M. Itano, D. J. Wineland, S. A. Diddams, L. Hollberg, E. A. Curtis, C. W. Oates, and Th. Udem. A mercury-ion optical clock. In P. Gill, editor, *Proceedings of the 6th symposium on frequency standards and metrology*, page 99, Singapore, 2002. World Scientific.

[31] D. J. Berkeland and M. G. Boshier. Destabilization of dark states and optical spectroscopy in zeeman-degenerate atomic systems. *Phys. Rev. A*, 65:033413, 2002.

[32] B. King. *Quantum state engineering and information processing with trapped ions.* PhD thesis, University of Colorado, 1999.

[33] C. F. Roos. *Controlling the quantum state of trapped ions.* PhD thesis, Universität Innsbruck, 2000.

[34] T. Schaetz, M. D. Barrett, D. Leibfried, J. Britton, J. Chiaverini, W. M. Itano, J. D. Jost, E. Knill, C. Langer, and D. J. Wineland. Enhanced quantum state detection efficiency through quantum information processing. *Phys. Rev. Lett.*, 94:010501, 2005.

[35] J. Metcalf and P. van der Straten. *Laser Cooling and Trapping.* Springer, Stony Brook, NY, 1999.

[36] L. Deslauriers, P. C. Haljan, P. J. Lee, K-A. Brickman, B. B. Blinov, M. J. Madsen, and C. Monroe. Zero-point cooling and low heating of trapped $^{111}cd^+$ ions. *Phys. Rev. A*, 70(4):043408, 2004.

[37] U. Tanaka, H. Imajo, K. Hayasaka, R. Ohmukai, M. Watanabe, and S. Urabe. Determination of the ground-state hyperfine splitting of trapped $^{113}cd^+$ ions. *Phys. Rev. A*, 53:3982, 1996.

[38] D. L. Moehring, B. B. Blinov, D. W. Gidley, R. N. Kohn, Jr., M. J. Madsen, T. D. Sanderson, R. S. Vallery, and C. Monroe. Precision lifetime measurement of a single trapped ion with fast laser pulses. *Phys. Rev. A*, 76:023413, 2006.

[39] M. J. Madsen, D. L. Moehring, P. Maunz, R. N. Kohn, Jr., L.-M. Duan, and C. Monroe. Ultrafast coherent coupling of atomic hyperfine and photon frequency qubits. *Phys. Rev. Lett.*, 97:040505, 2006.

[40] M. Keller, B. Lange, K. Hayasaka, W. Lange, and H. Walther. Continuous generation of single photons with controlled waveform in an ion-trap cavity system. *Nature*, 431:1075, 2004.

[41] C. Langer, R. Ozeri, J. D. Jost, J. Chiaverini, B. DeMarco, A. Ben-Kish, R. B. Blakestad, J. Britton, D. B. Hume, W. M. Itano, D. Leibfried, R. Reichle, T. Rosenband, T. Schaetz, P. O. Schmidt, and D. J. Wineland. Long-lived qubit memory using atomic ions. *Phys. Rev. Lett.*, 95:060502, 2005.

[42] Chr. Tamm, D. Engelke, and V. Bühner. Spectroscopy of the electric-quadrupole transition $^2s_{1/2}$(f=0) - $^2d_{3/2}$(f=2) in trapped $^{171}yb^+$. *Phys. Rev. A*, 61:053405, 2000.

[43] S. Olmschenk, K. C. Younge, D. L. Moehring, D. Matsukevich, P. Maunz, and C. Monroe. Manipulation and detection of a trapped yb^+ hyperfine qubit. *Phys. Rev. A*, 76:052314, 2007.

[44] D. Engelke and Chr. Tamm. Dark times in the resonance fluorescence of trapped ^{171}yb ions caused by spontaneous quantum jumps to the $^2d_{3/2}$(f=2) state. *Europhys. Lett.*, 33:347, 1996.

[45] M. G. Raizen, J. M. Gilligan, J. C. Bergquist, W. M. Itano, and D. J. Wineland. Linear trap for high-accuracy spectroscopy of stored ions. *J. Mod. Opt.*, 39:233, 1992.

[46] http://www.emccd.com/index.html.

[47] K.-A. Brickman. *Implementation of Grover's Quantum Search Algorithm with Two Trapped Ions.* PhD thesis, University of Michigan, 2007.

[48] M. J. Madsen, W. K. Hensinger, D. Stick, J. A. Rabchuk, and C. Monroe. Planar ion trap geometry for microfabrication. *Applied Physics B: Lasers and Optics*, 78(5):639 – 651, 2004.

[49] M. J. Madsen. *Advanced Ion Trap Development and Ultrafast Laser-Ion Interactions.* PhD thesis, University of Michigan, 2006.

[50] D. Hucul, M. Yeo, W. K. Hensinger, J. Rabchuk, S. Olmschenk, and C. Monroe. On the transport of atomic ions in linear and multidimensional ion trap arrays. *QIC*, 8:501–578, 2008.

[51] D. E. Pritchard, E. L. Raab, V. Bagnato, C. E. Wieman, and R. N. Watts. Light traps using spontaneous forces. *Phys. Rev. Lett.*, 57:310313, 1986.

[52] E. Raab, M. Prentiss, A. Cable, S. Chu, and D. Pritchard. Trapping of neutral sodium atoms with radiation pressure. *Phys. Rev. Lett.*, 59:2631, 1987.

[53] M. H. Anderson, J. R. Ensher, M. R. Matthews, C. E. Wieman, and E. A. Cornell. Observation of bose-einstein condensation in a dilute atomic vapor. *Science*, 269:198, 1995.

[54] M. Greiner, C. A. Regal, and D. S. Jin. Emergence of a molecular bose-einstein condensate from a fermi gas. *Nature*, 426:537, 2003.

[55] J. A. Sauer, K. M. Fortier, M.-S. Chang, C. D. Hamley, and M. S. Chapman. Cavity qed with optically transported atoms. *Phys. Rev. A*, 69:051804(R), 2004.

[56] C. W. Hoyt, Z. W. Barber, C. W. Oates, T. M. Fortier, S. A. Diddams, and L. Hollberg. Observation and absolute frequency measurements of the $^1s_0$-$^3p_0$ optical clock transition in neutral ytterbium. *Phys. Rev. Lett.*, 95:083003, 2005.

[57] J. Weiner, V. S. Bagnato, S. Zilio, and P. S. Julienne. Experiments and theory in cold and ultracold collisions. *Rev. Mod. Phys.*, 71(1):1–85, Jan 1999.

[58] G. Raithel, O. Benson, and H. Walther. Atomic interference in the one-atom-maser. *Phys. Rev. Lett.*, 75:3446, 1995.

[59] A. J. Leggett. Bose-einstein condensation in the alkali gases: Some fundamental concepts. *Rev. Mod. Phys.*, 73(2):307–356, Apr 2001.

[60] C. W. Oates, F. Bondu, R. W. Fox, and L. Hollberg. A diode-laser optical frequency reference based on laser-cooled ca atoms. *Eur. Phys. J. D*, 7:449, 1999.

[61] K. Sengstock, U. Sterr, V. Rieger, D. Bettermann, J. H. Müller, and W. Ertmer. Optical ramsey spectroscopy on laser trapped and thermal mg-atoms. *Appl. Phys. B*, 59:99, 1994.

[62] X. Xu, T. H. Loftus, M. J. Smith, J. L. Hall, A. Gallagher, and J. Ye. Dynamics in a two-level atom magneto-optical trap. *Phys. Rev. A*, 66(1):011401, Jul 2002.

[63] C. Y. Park and T. H. Yoon. Efficient magneto-optical trapping of yb atoms with a violet laser diode. *Phys. Rev. A*, 68(5):055401, Nov 2003.

[64] M. Cetina, A. Grier, J. Campbell, I. Chuang, and V. Vuletic. Bright source of cold ions for surface-electrode traps. *Phys. Rev. A*, 97:041401(R), 2007.

[65] R. Côté, V. Kharchenko, and M. D. Lukin. Mesoscopic molecular ions in bose-einstein condensates. *Phys. Rev. Lett.*, 89(9):093001, Aug 2002.

[66] Z. Idziaszek, T. Calarco, and P. Zoller. Controlled collisions of a single atom and ion guided by movable trapping potentials. *Phys. Rev. A*, 76:033409, 2007.

[67] K. L. Corwin, Z.-T. Lu, C. F. Hand, R. J. Epstein, and C. E. Wieman. Frequency stabilized diode laser using the zeeman shift in an atomic vapor. *Appl. Opt.*, 37:3295, 1998.

[68] J. M. Reeves, O. Garcia, and C. A. Sackett. Temperature stability of a dichroic atomic vapor laser lock. *Appl. Opt.*, 45:372, 2006.

[69] C. Monroe, W. Swann, H. Robinson, and C. Wieman. Very cold trapped atoms in a vapor cell. *Phys. Rev. Lett.*, 65(13):1571–1574, Sep 1990.

[70] D. Hoffmann, P. Feng, and T. Walker. Measurements of rb trap-loss collision spectra. *J. Opt. Soc. Am. B*, 11:712, 1994.

[71] M. S. Santos, P. Nussenzveig, L. G. Marcassa, K. Helmerson, J. Flemming, S. C. Zilio, and V. S. Bagnato. Simultaneous trapping of two different atomic species in a vapor-cell magneto-optical trap. *Phys. Rev. A*, 52(6):R4340–R4343, Dec 1995.

[72] T. P. Dinneen, K. R. Vogel, E. Arimondo, J. L. Hall, and A. Gallagher. Cold collisions of $sr*-sr$ in a magneto-optical trap. *Phys. Rev. A*, 59(2):1216–1222, Feb 1999.

[73] K. Lindquist, M. Stephens, and C. Wieman. Experimental and theoretical study of the vapor-cell zeeman optical trap. *Phys. Rev. A*, 46(7):4082–4090, Oct 1992.

[74] K. E. Gibble, S. Kasapi, and S. Chu. Improved magneto-optic trapping in a vapor cell. *Opt. Lett.*, 17:526, 1992.

[75] T. Walker, D. Sesko, and C. Wieman. Collective behavior of optically trapped neutral atoms. *Phys. Rev. Lett.*, 64(4):408–411, Jan 1990.

[76] D. N. Madsen and J. W. Thomsen. Measurement of absolute photo-ionization cross sections using magnesium magneto-optical traps. *J. Phys. B*, 35:2173, 2002.

[77] L. Deslauriers, S. Olmschenk, D. Stick, W.K. Hensinger, J. Sterk, and C. Monroe. Scaling and suppression of anamolous quantum decoherence in ion traps. *Phys. Rev. Lett.*, 97:103007, 2006.

[78] R. R. Adzhimambetov, A. T. Tursunov, and É. É. Khalilov. Study of the cds crystal evaporation kinetics by laser step atomic photoionization. *Tech. Phys.*, 48:1020, 2003.

[79] L.-W. He, C. E. Burkhardt, M. Ciocca, J. J. Leventhal, and S. T. Manson. Absolute cross sections for the photoionization of the 6s6p 1p excited state of barium. *Phys. Rev. Lett.*, 67(16):2131–2134, Oct 1991.

[80] E. Aucouturier, N. Dimarcq, P. Petit, C. Valentin, and S. Weyers. The l.h.a. 2d magneto-optical trap: On the way to a continuous beam of cold atoms. In *Eur. Freq. Time Forum*, page 230, 1996.

[81] M. Chevrollier, E. G. Lima, O. Di Lorenzo, A. Lezama, and M. Oriá. Magneto-optical trap near a surface. *Opt. Comm.*, 136:22, 1996.

[82] N. W. M. Ritchie, E. R. I. Abraham, and R. G. Hulet. Trap loss collisions of ^{7}li: The role of trap depth. *Laser Phys.*, 4:1066, 1994.

[83] S. D. Gensemer, V. Sanchez-Villicana, K. Y. N. Tan, T. T. Grove, and P. L. Gould. Trap-loss collisions of ^{85}rb and ^{87}rb: Dependence on trap parameters. *Phys. Rev. A*, 56:4055, 1997.

[84] J. M. Kohel, J. Ramirez-Serrano, R. J. Thompson, L. Maleki, J. L. Bliss, and K. G. Libbrecht. Generation of an intense cold-atom beam from a pyramidal magento-optical trap: experiment and simulation. *J. Opt. Soc. Am. B*, 20:1161, 2003.

[85] J. Kim, S. Pau, Z. Ma, H. R. McLellan, J. V. Gates, A. Kornblit, R. E. Slusher, R. Jopson, I. Kang, and M. Dinu. System design for a large-scale ion trap quantum information processor. *QIC*, 5:515, 2005.

[86] D. Stick, W. K. Hensinger, S. Olmschenk, M. J. Madsen, K. Schwab, and C. Monroe. Ion trap in a semiconductor chip. *Nature Physics*, 2:36, 2006.

[87] S. Seidelin, J. Chiaverini, R. Reichle, J. J. Bollinger, D. Leibfried, J. Britton, J. H. Wesenberg, R. B. Blakestad, R. J. Epstein, D. B. Hume, J. D. Jost, C. Langer, R. Ozeri, N. Shiga, and D. J. Wineland. A microfabricated surface-electrode ion trap for scalable quantum information processing. *Phys. Rev. Lett.*, 96:253003, 2006.

[88] J. Flemming, L. G. Marcassa, R. J. Horowicz, S. C. Zilio, and V. S. Bagnato. Enhanced loading of a two-color vapor-cell magneto-optical trap for sodium atoms. *Opt. Lett.*, 20:2529, 1995.

[89] V. Vuletic, C. Zimmermann, and T. W. Hansch. Steep magnetic trap for ultra cold atoms. *Europhys. Lett.*, 36:349, 1996.

[90] M. Born and E. Wolf. *Principles of Optics: Electromagnetic theory of propagation, interference and diffraction of light.* Cambridge University Press, Cambridge, UK, 7th edition, 2002.

[91] P. L. Ramazza, S. Ducci, A. Zavatta, M. Bellini, and F. T. Arecchi. Second-harmonic generation from a picosecond ti:sa laser in lbo: conversion efficiency and spatial properties. *Appl. Phys. B*, 75:53, 2002.